PLANT SCIENCES

MAcro Plant Projection Imaging (MAPPI): An open, scalable platform for whole-plant fluorescence real-time imaging

Giorgia Tortora[1]†, Bianca Maria Orlando Marchesano[2]†, Stefano Buratti[2,3], Laura Luoni[2], Matteo Grenzi[2], Keiko Yoshioka[4], Valeria Contartese[5], Alessia Candeo[1], Alex Costa[2,6]*, Andrea Bassi[1]*

Understanding how plants perceive and respond to environmental and developmental cues requires tools capable of monitoring molecular signals in vivo, across whole tissues, and in real time. Genetically encoded fluorescent indicators, coupled with fluorescence microscopy, have transformed plant biology, but their application remains largely confined to small model organisms and specialized microscopy instrumentation. Here, we present MAcro Plant Projection Imaging (MAPPI), an open-source, low-cost, and modular fluorescence imaging platform for soil-grown plants beyond the model organism or seedling stage. MAPPI enables wide field-of-view, dual-projection imaging of fluorescent reporters, supporting real-time visualization of systemic signals under near-physiological conditions. We validate MAPPI by tracking calcium and L-glutamate dynamics in adult *Nicotiana benthamiana* plants, revealing developmentally regulated long-distance calcium waves triggered by wounding, burning, or submergence, including bidirectional shoot-to-root and root-to-shoot signaling. By democratizing access to whole-plant functional imaging, MAPPI provides a scalable tool for dissecting signal propagation, stress adaptation, and systemic communication in both model and nonmodel species.

INTRODUCTION

Advancements in genetic and molecular biology tools have revolutionized the study of plant biology, enabling unprecedented insights into plant physiology and signaling. The development of plants expressing genetically encoded fluorescent indicators (GEFIs), such as for calcium (Ca^{2+}), potassium (K^+), pH, phytohormones, and redox-sensitive indicators, coupled with fluorescence microscopy has transformed in vivo studies of plant signaling (*1*–*4*). Particularly, the continuous evolution of GEFIs and imaging technologies has enabled real-time visualization of second messengers (e.g., Ca^{2+}) and signaling molecules [e.g., reactive oxygen species (ROS) and redox couples] from subcellular compartments to organs like leaves and roots, up to whole small plants (*1*, *3*, *5*–*7*).

Among these signaling elements, Ca^{2+} is widely recognized as crucial second messenger in both unicellular and multicellular organisms (*8*, *9*). In plants, beyond serving as an essential structural element (*10*), Ca^{2+} orchestrates diverse signaling pathways in response to developmental cues and environmental stresses (*11*–*13*). Biotic and abiotic stimuli trigger transient increases in cytosolic and organellar Ca^{2+} concentration (*14*–*18*). For the past two decades, these dynamics have been primarily investigated through wide-field and confocal fluorescence microscopy (*4*, *6*), often using Ca^{2+} indicators, such as the Förster resonance energy transfer (FRET)–based Yellow Cameleon YC3.6, which requires advanced microscopy setups equipped with dual cameras or photomultipliers (*6*). As a result, most studies have focused on highly accessible systems such as pollen tubes, root hairs, or stomata guard cells (*19*–*24*). More recently, the introduction of intensiometric Ca^{2+} indicators, such as GCaMP and GECO (*25*–*27*), has enabled Ca^{2+} imaging using simpler, single-camera fluorescence microscopes, including wide-field and stereo (*28*–*30*). These tools have facilitated the visualization of Ca^{2+} dynamics in seedlings and whole adult *Arabidopsis thaliana* plants (*30*–*35*). Notably, the use of GCaMP3 Ca^{2+} indicator demonstrated the utility of stereo fluorescence microscopes with relatively large field of view (FOV) to track long-distance Ca^{2+} waves traveling leaf-to-leaf in response to mechanical stress or herbivory (*31*, *32*). These discoveries ushered in an era of research into the study of how plants generate and propagate long-distance Ca^{2+} signals, underscoring their importance in coordinating whole-plant responses to injury and in advancing our understanding of rapid systemic defense and stress acclimation processes (*36*, *37*).

While most of this progress has focused on *A. thaliana*, the increased sensitivity of modern GEFIs should enable studies in larger, nonmodel species of agronomic interest (e.g., *Solanum lycopersicum* and *Solanum tuberosum*). However, moving beyond *A. thaliana* requires not only the generation of transgenic lines expressing the GEFIs but also imaging platforms capable of accommodating the larger size and more complex morphology of adult plants. Commercial solutions are typically expensive, low in modularity, and limited in FOV or flexibility.

To address these limitations, we developed the MAcro Plant Projection Imaging (MAPPI) system, a low-cost, modular, fluorescence imaging setup tailored for dual-view whole-plant visualization in soil-grown specimens larger than *A. thaliana*. We validated the MAPPI system using *Nicotiana benthamiana* plants expressing the GCaMP3 Ca^{2+} indicator (*29*). The large FOV and the ability to

[1]Department of Physics, Politecnico di Milano, Piazza Leonardo da Vinci, 20133 Milan, Italy. [2]Department of Biosciences, Università degli Studi di Milano, Via G. Celoria 26, 20133 Milan, Italy. [3]Fratelli Confalonieri Foundation, via Vincenzo Monti 25, 20123 Milan, Italy. [4]Department of Cell and Systems Biology, University of Toronto, Toronto, ON, Canada. [5]Research and Development Department, Green Has Italia S.p.A, Canale, Cuneo, Italy. [6]Institute of Biophysics, Consiglio Nazionale delle Ricerche, 20133 Milan, Italy.
*Corresponding author. Email: alex.costa@unimi.it (A.C.); andrea1.bassi@polimi.it (A.B.)
†These authors contributed equally to this work.

simultaneously image the specimen from two distinct views allowed us to visualize, in real time, cytosolic Ca^{2+} waves from shoot-to-root and root-to-shoot in adult plants. This capability enables the investigation of key aspects of plant signaling, including the conservation of long-distance Ca^{2+} wave propagation beyond *A. thaliana*, the spatial extent and limitations of signal transmission within the plant body, and the developmental regulation of these responses. MAPPI also enables monitoring of apoplastic L-glutamate dynamics in *N. benthamiana*, suggesting that its role as a signaling molecule in the response to mechanical damage is conserved beyond *A. thaliana*.

By integrating this optical platform with open-source tools for data acquisition, signal quantification, and detailed hardware assembly guidelines, MAPPI empowers researchers to explore these questions in large plants using real-time imaging of genetically encoded indicators under environmentally relevant conditions.

RESULTS

Large FOV imaging of adult plants with the MAPPI system

Our recent research has focused on the study of long-distance Ca^{2+} signal propagation in *A. thaliana* plants in response to leaf mechanical stimuli such as wounding, burning, and osmotic stress (*34*). This area of research was pioneered by Gilroy and Farmer labs who first reported the use of *A. thaliana* plants expressing the GCaMP3 Ca^{2+} indicators imaged with a fluorescence stereo microscope (*31*, *32*). In addition, other laboratories demonstrated the existence of long-distance Ca^{2+} waves in adult *A. thaliana* plants in response to salt stress and wounding, using aequorin-based indicators and sensitive imaging systems (*38*, *39*). Nevertheless, aside from the novelty of their works, a closer examination of published images reveals a substantial limitation: In most cases, the acquired images captured seedlings grown on agar plates or only portions of mature plants (*40*).

In our own efforts to study long-distance systemic Ca^{2+} wave propagation in *A. thaliana* (*34*), we encountered similar limitations, prompting us to pose three key questions: (i) Is the propagation of mechanically induced Ca^{2+} waves conserved across plant species? (ii) What is the spatial extent of these long-distance signals within a plant? (iii) Is this signaling mechanism developmentally regulated?

To address these questions, we recognized the need to adopt a model plant different from *A. thaliana*. The development of *N. benthamiana* plants expressing GCaMP3 (*29*) provides an ideal alternative. *N. benthamiana* plants offer the potential to explore these questions in a larger plant model and to deepen our understanding of long-distance Ca^{2+} signaling. In their original work, DeFalco and colleagues showed that stimuli like leaf wounding, cold shock, external adenosine 5′-triphosphate, L-glutamate, and pathogen elicitors were able to induce cytosolic Ca^{2+} increases in leaf discs of GCaMP3 *N. benthamiana* plants. However, by using leaf discs, they limited their observations to local responses. Because we were interested in determining whether, in *N. benthamiana*, wounding-induced long-distance Ca^{2+} waves are present, we imaged two-leaf-stage (comprising two cotyledons and two true leaves) soil-grown tobacco plants with a commercial fluorescence stereo microscope (Nikon SMZ18), a developmental stage at which the entire plant fit within the FOV of the instrument (fig. S1). The wounding of one leaf using a tweezer clearly and reliably induced a cytosolic Ca^{2+} increase in the local leaf generating a long-distance Ca^{2+} wave propagating to the petiole up to the systemic leaves and cotyledons (fig. S1). Thus, we observed that, at this developmental stage, leaf wounding in *N. benthamiana* induces long-distance Ca^{2+} waves propagating at a speed of 1.3 ± 0.26 mm/s, comparable to values reported in *A. thaliana* plants (*31*, *32*).

Whereas our first question was answered by this experiment, the other questions could not be appropriately addressed because of the need to perform experiments with plants at different developmental stages, hence with a larger size. A 5- to 6-week-old *N. benthamiana* plant with five to seven or more leaves has an average diameter of around 14 cm with a height of around 9 cm. Because the maximum FOV of a typical stereomicroscope is of a few centimeters, even if it can accommodate plants at this stage, it cannot provide a complete view with a sufficient focus of the entire plant. Thus, this limitation prevented us from answering our questions and motivated us to develop a custom-made large fluorescence imaging setup that we named MAcro Plant Projection Imaging (MAPPI).

To design the MAPPI setup, we established several key requirements: (i) a FOV larger than that of conventional stereomicroscopes; (ii) sufficient excitation power to induce fluorescence across the entire shoot of adult plants from various species; (iii) uniform and homogeneous fluorescence illumination; (iv) a sensitive camera paired with appropriate optical filters to detect GCaMP3 fluorescence while minimizing chlorophyll autofluorescence; and (v) a system that is simple to build and operate, cost-effective, and easily replicable. To achieve these goals, we opted for the implementation of commercially available high-power light-emitting diode (LED), machine vision objective, and complementary metal-oxide semiconductor (CMOS) camera. The LED is composed of four emitters providing enhanced power compared to standard LEDs and assuring enough energy to induce fluorescence over a large area, while the machine vision objective, used in combination with 1/1.2 inches (13.33 mm) camera sensor (1920×1200 pixels), offers a FOV which spans 46° (corresponding to 19 cm by 13 cm in a typical setting). A system of lenses integrated into the LED cage creates a homogeneous illumination plane right outside the LED cage itself, which is controlled in size by a manual diaphragm. An additional lens added to the illumination path conjugates this plane with the sample, allowing the formation of an enlarged uniform illumination area at the sample (Fig. 1A). The detection field can be matched to the illumination footprint, which itself is tunable based on the specimen's size. With the diaphragm fully open, the illumination covers a circular area of about 20 cm in diameter. By adjusting the camera's distance, a similar FOV can be achieved while maintaining the sample in focus. Besides enabling the observation of the entire shoot of relatively large plants (Fig. 1A), the obtained FOV enables for the accommodation of multiple samples simultaneously (Fig. 1B), hence giving the opportunity to perform experiments on several plants in parallel. Last, the illumination and detection units are both mounted on a vertical shaft with adjustable clamping platforms, allowing the distance between the setup and the sample to be easily modified on the basis of the plant's size. This feature is crucial as the system must allow imaging of the entire shoot of plants across various species and developmental stages, which naturally vary in size and conformation. Once the imaging setup was ready, we performed preliminary experiments on *N. benthamiana* plants expressing the GCaMP3 Ca^{2+} indicator to identify the best acquisition parameters, which would have allowed obtaining a sufficiently high fluorescence signal while reducing signal-to-noise ratio, maintaining acceptable exposure and sampling times. The LED power was set at its maximum directly using the LED dimmer, obtaining an irradiance of 7.6 mW/cm^2 at the sample, while a good compromise for the exposure

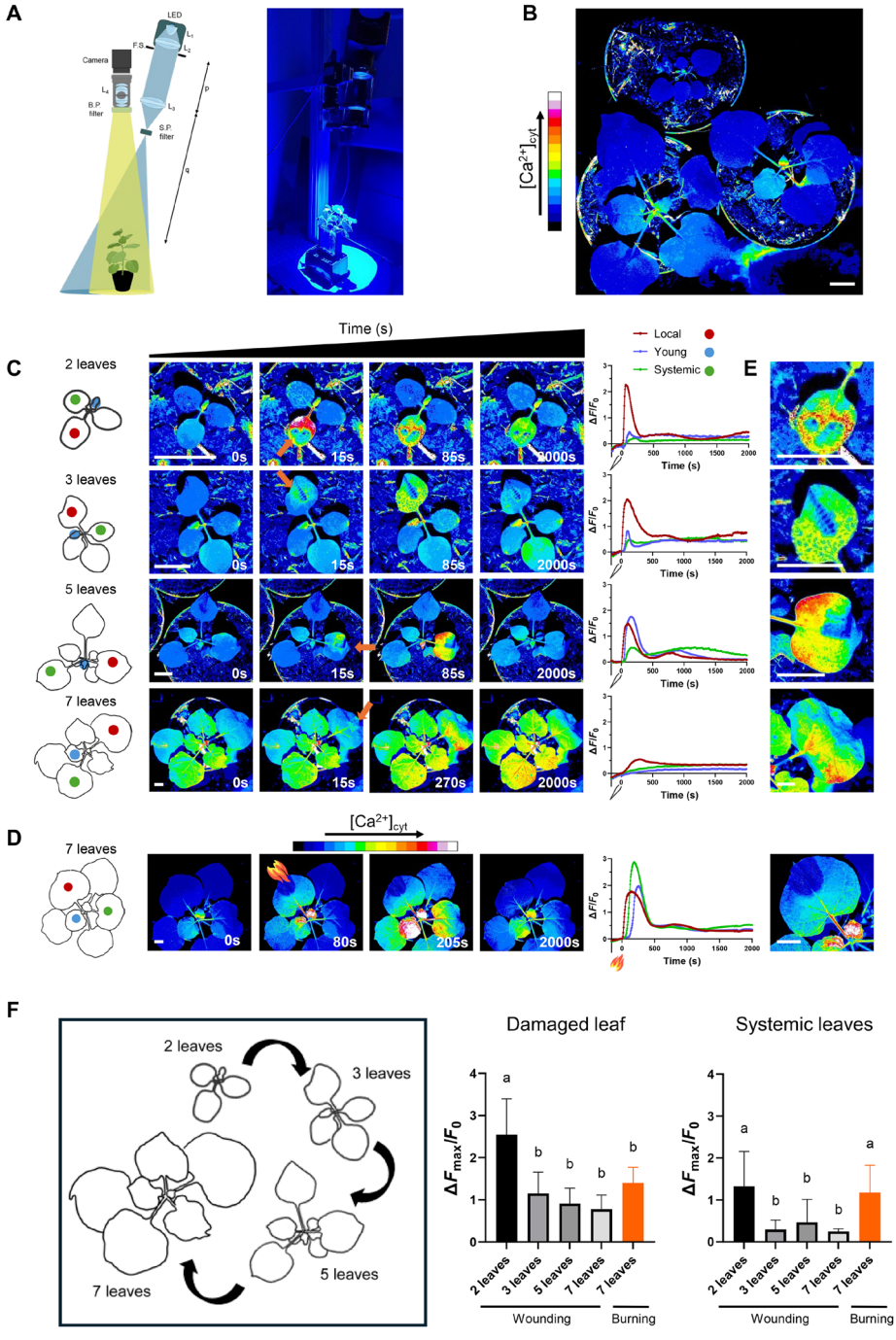

Fig. 1. Propagation of cytosolic Ca^{2+} signals in *N. benthamiana* leaves after press wounding and leaf burning. (**A**) Scheme and photograph of the MAPPI system. (**B**) Simultaneous imaging of three plants at the 5-leaf-stage expressing the GCaMP3 Ca^{2+} indicator. Scale bar, 1 cm. (**C**) Left: Schematic of plants at different developmental stages. Colored dots mark leaves used for GCaMP3 quantification: damaged (red), young (blue), and systemic (green). Center: Representative false-color images (16-color lookup table) before and after wounding. Arrows indicate the wounded leaf. Scale bars, 1 cm. Right: Normalized GCaMP3 fluorescence traces ($\Delta F/F_0$) from one representative plant for each stage (2-, 3-, 5-, and ≥7-leaf stage). (**D**) Left: Schematic of plants at the selected ≥7-leaf stage. Colored dots mark quantified leaves. Center: False-color images before and after burning; the flame icon marks the burned leaf. Scale bar, 1 cm. Right: Normalized $\Delta F/F_0$ traces from one representative plant. Note: The same representative plant shown in fig. S4A is used here to illustrate systemic signal propagation across multiple leaves following burning. (**E**) Enlarged views of damaged leaves for wounding (top) and burning (bottom). Images correspond to 85 s (2-, 3-, and 5-leaf stage), 270 s (≥7-leaf-stage wounding), and 205 s (≥7-leaf-stage burning). Scale bars, 0.5 cm for the two-leaf-stage sample and 1 cm for all others. (**F**) Left: Schematic of developmental stages analyzed. Right: Maximal normalized fluorescence changes ($\Delta F_{max}/F_0$) in local (left box) and systemic (right box) leaves after wounding or burning. Error bars, SD. Different letters denote significant differences [one-way analysis of variance (ANOVA), $P \leq 0.05$]; $n \geq 7$ plants. Exposure time, 500 ms. Sampling interval, 5 s. Total acquisition, 35 min. Wounding and burning were applied 3 min after the acquisition started. F.S., field stop; B.P., band pass filter; S.P., short pass filter; L1, Lens 1; L2, Lens 2; L3, Lens 3; L4, Lens 4.

time was found in setting it to 500 ms. On the basis of previous studies (*31*–*34*), we adopted a temporal resolution of 3 and 5 s for *A. thaliana* and *N. benthamiana*, respectively, using a 500-ms exposure time, which is sufficient to capture the spatial and temporal characteristics of Ca^{2+} wave propagation while minimizing data redundancy and phototoxic effects. We then characterized the spatial and temporal resolution of the system. Using a sharp-edge measurement, we estimated the system's spatial resolution to be ~360 μm. Together, these developments laid the foundation for a dedicated imaging platform capable of overcoming the FOV and resolution limitations of conventional systems, ultimately enabling real-time, whole-plant monitoring of systemic Ca^{2+} dynamics in nonmodel plants such as adult *N. benthamiana*.

Wound-induced Ca^{2+} signal propagation in *N. benthamiana* plants at different developmental stages

MAPPI enables imaging of adult *N. benthamiana* plants by detecting GCaMP3 fluorescence with an exposure time and a frame rate, which should be compatible with the temporal resolution required to capture both local and systemic cytosolic Ca^{2+} dynamics (*29*, *31*–*34*). Thus, we evaluated the sensitivity of the MAPPI system in detecting changes in GCaMP3 fluorescence dependent on cytosolic Ca^{2+} increases. To this end, we wounded the leaves of plants at the two-leaf stage, the same stage used in experiments with the stereomicroscope (fig. S1). Following wounding, we observed a clear and transient increase in GCaMP3 fluorescence close to the wounded area (Fig. 1C) followed by the emergence of a Ca^{2+} wave propagating through the main vasculature toward distal regions (Fig. 1C and movie S1). Quantitative analysis revealed a normalized GCaMP3 fluorescence change ($\Delta F/F_0$) of 2.5 ± 0.81 in the wounded leaf and 1.32 ± 0.8 in the systemic leaf (Fig. 1C). These values are almost double to those obtained with the stereomicroscope (0.95 ± 0.25 for the local and 0.49 ± 0.13 for the systemic) (fig. S1), suggesting that the MAPPI may offer improved sensitivity in detecting dynamic fluorescence signals. These results demonstrate that the sensitivity of the MAPPI system is comparable to, and possibly exceeds, that of conventional stereomicroscope while additionally offering a much larger FOV. We leveraged this capability to investigate whether long-distance Ca^{2+} waves occur in older *N. benthamiana* plants and whether they can travel from local to systemic leaves. Our goal was to reveal systemic signaling events that would, otherwise, remain undetectable with conventional imaging systems. We examined plants at three different developmental stages: 3, 5, and ≥7 true leaves (as illustrated in the left-hand schematics of Fig. 1C). To maintain a consistent ratio between the wounded leaf surface and the total leaf area, we incrementally increased the injury using custom-designed three-dimensionally (3D) printed tweezers (see Materials and Methods and fig. S2D). At all developmental stages, in the local leaf, we observed the typical increase in GCaMP3 fluorescence in the vascular and intervascular tissues near the wound site (Fig. 1E). However, long-distance Ca^{2+} waves propagating to systemic leaves were only detected in plants at the 3- and 5-leaf stages. In ≥7-leaf-stage plants, only minimal fluorescence changes were observed (Fig. 1C and movie S1; average of wounded area was around 3 cm^2, which corresponds to ~11% of the total leaf area). Qualitative analysis of fluorescence changes across developmental stages revealed that signal intensity gradually decreases both locally (in the wounded leaf) and systemically (Fig. 1, C and F, and fig. S3). Exposure to blue light alone resulted in only a modest fluorescence increase, substantially lower than the fluorescence change observed upon wounding (fig. S3F and movie S2). This response can likely be attributed to the use of a blue light excitation source, which is known to induce cytosolic Ca^{2+} increases (*41*–*43*). These findings suggest that the attenuation, and eventual absence, of long-distance systemic Ca^{2+} waves, is associated with a reduced magnitude of the local response (Fig. 1, C and F; fig. S3, A to D; and movie S1). This observation aligns with the known properties of wounding-induced slow wave potentials, a phenomenon strictly intertwined with Ca^{2+} waves (*31*), which differ from action potentials in that they are not all-or-nothing responses and depend on the strength of the initial triggering stimulus (*44*–*47*). Notably, even if larger tweezers were used for bigger leaves, the strength of the applied stimulus might not scale proportionally. Overall, our results indicate that wounding-induced long-distance Ca^{2+} waves are present in adult *N. benthamiana*, and their systemic propagation from leaf to leaf depends on the plant's size.

Systemic Ca^{2+} wave propagation in ≥7-leaf-stage *N. benthamiana* plants is observed in response to leaf burning

To see whether the long-distance Ca^{2+} propagation from leaf to leaf still occurs in older *N. benthamiana* plants we decided to assess the response to a mechanical stress stronger than wounding, like leaf burning. Burning the leaf or stem of different plant species reliably triggers slow wave potentials initiation and propagation (*45*, *48*–*53*), and we recently showed that burning a single rosette leaf of adult *A. thaliana* plants triggers a long-distance Ca^{2+} wave that propagates throughout the entire basal rosette and all the way to the primary inflorescence, tens of centimeters away from the injured tissues (*34*). Because, in ≥7-leaf-stage *N. benthamiana* plants, wounding failed to induce an increase in cytosolic Ca^{2+} in systemic tissues (Fig. 1C and fig. S3D), we evaluated the response to a stronger mechanical stimulus by applying localized leaf burning using a lighter (Fig. 1D and movie S3). The average burned area was 4.46 cm^2 (~17.4% of the total leaf area). Burning the leaf resulted in a normalized GCaMP3 fluorescence increase of 1.4 ± 0.3 in the local, not-damaged tissue (Fig. 1, D to F, and fig. S3E) and also triggered a marked fluorescence increase in systemic leaves (Fig. 1, D and F; fig. S3E; and movie S3) with a normalized GCaMP3 fluorescence increase of 1.2 ± 0.2, a value significantly higher than that observed in systemic leaves of ≥7-leaf-stage wounded plants (0.28 ± 0.08) (Fig. 1, D and F; and fig. S3, D and E). By plotting normalized GCaMP3 fluorescence changes over time, we observed that the Ca^{2+} wave propagated across systemic leaves with a mean propagation speed of 1.72 ± 0.65 mm/s, but the propagation was not simultaneous across all the systemic leaves (Fig. 1D and movie S3). We also observed a delay in the response between the two halves of systemic leaves: the half closer to the burnt leaf exhibited a faster response compared to the distal half (fig. S4, A and B, and movie S3). This finding was reported in 31 leaves of the 41 analyzed (75.6%), while 10 of the 41 leaves (24.4%) did not show a delay between the two halves (fig. S4C).

Overall, our results confirm that long-distance Ca^{2+} waves can still be generated in ≥7-leaf-stage plants but require a sufficiently strong stimulus. Such activation can be reliably triggered by specific types of stimuli, such as leaf burning. Furthermore, different leaves exhibited distinct timing and asymmetrical GCaMP3 fluorescence responses, reminiscent of observations in adult *A. thaliana* plants grown in short day conditions, where the wounding of "leaf 8"

generates long-distance slow wave potentials and Ca^{2+} signals that propagate to "leaf 13" but not "leaf 9," suggesting a dependence on vascular connectivity (*31*, *54*). To our knowledge, the delayed response between the two halves of a single leaf has not been previously reported.

In conclusion, MAPPI enabled the detection of systemic Ca^{2+} waves propagating from leaf to leaf in *N. benthamiana* during all stages of development. However, in older plants, this response required a strong stimulus such as leaf burning, as wounding alone was insufficient to induce long-distance signaling, suggesting that mechanical damage from insect chewing may not be adequate to trigger systemic Ca^{2+} waves. To test this hypothesis, we applied *Spodoptera littoralis* larvae to the leaves of ≥7-leaf-stage *N. benthamiana* plants expressing GCaMP3. The effect of larvae chewing triggered a significant cytosolic Ca^{2+} increase in the local chewed leaf, with no Ca^{2+} waves propagating to systemic tissues (movie S4). Our results, enabled by the large FOV of the MAPPI system, are consistent with a localized rather than systemic response. Long-distance Ca^{2+} wave propagation is not necessarily activated by mild biotic stimuli like insect feeding.

Local and systemic apoplastic L-glutamate accumulation occurs in adult *N. benthamiana* plants in response to leaf wounding and burning

In the previous section, we reported the conservation of wounding- and burning-induced long-distance Ca^{2+} waves in *N. benthamiana* plants using the MAPPI system. In *A. thaliana*, it has been reported that long-distance Ca^{2+} signals are primarily mediated by L-glutamate receptor-like channel 3.3 (GLR3.3) and GLR3.6 (*31*, *32*, *34*). In particular, we have previously showed that the binding of L-glutamate to GLR3.3 is required for the in planta activation of the GLR3.3 channel (*34*, *55*). An increase in apoplastic L-glutamate concentration has been observed both in local tissues directly subjected to wounding (*32*, *56*) and in systemic tissues (*34*), suggesting that, in *A. thaliana*, L-glutamate acts as a signaling molecule being required for the GLR3.3 activation (*34*, *56*). On the basis of these observations, we investigated whether apoplastic L-glutamate levels also change in *N. benthamiana* following leaf damage.

To visualize synaptic L-glutamate dynamics in neurons in vivo, Marvin and colleagues developed the green-shifted fluorescent indicator for L-glutamate iGluSnFR (*57*), and, later, Toyota and colleagues targeted iGluSnFR to the apoplastic space and expressed it in *A. thaliana* plants (*32*). Because iGluSnFR shares the same excitation and emission properties as GCaMP3, we reasoned that the MAPPI system could be used to visualize apoplastic L-glutamate dynamics in *N. benthamiana* plants subject to mechanical stimulation. To this end, we generated *N. benthamiana* plants expressing iGluSnFR in the apoplast, using the construct by Toyota and colleagues (*32*), in which iGluSnFR is fused to CHIB (basic chitinase) signal peptide to ensure apoplastic localization. We successfully obtained *N. benthamiana* plants expressing iGluSnFR, and confocal analyses of leaf epidermal cells confirmed its proper apoplastic localization (fig. S5, B and D). We then followed the same experimental design to apply wounding and burning stimuli and used the MAPPI system configuration previously used to study Ca^{2+} dynamics. Leaf wounding triggered a rise in iGluSnFR fluorescence, indicative of increased apoplastic L-glutamate in the wounded leaf across plants of different developmental stages. However, the fluorescence change was markedly reduced in systemic leaves of 5- and ≥7-leaf-stage plants (Fig. 2A; fig. S6, A to C; and movie S5). In systemic leaves, a clear iGluSnFR fluorescence increase was observed only in 3-leaf-stage plants, suggesting that, similarly to what was observed for Ca^{2+} dynamics, the stimulus strength was insufficient to induce a detectable systemic response at later developmental stages. However, we detected a significant systemic increase in iGluSnFR fluorescence following leaf burning (Fig. 2B, fig. S6D, and movie S5). Similarly to what observed in *N. benthamiana* GCaMP3 plants, we observed a delay in the response between the two halves of systemic leaves also in iGluSnFR plants: 12 leaves of the 19 analyzed (63.16%) reported a delay, while 7 of the 19 leaves (36.84%) did not show a delay between the two halves (fig. S7). Exposure to blue light alone resulted in only a modest fluorescence increase, substantially lower than the fluorescence change observed upon wounding or burning (fig. S6E and movie S6). These results extend the observations in *A. thaliana*, supporting the notion that apoplastic L-glutamate accumulation occurs both locally and systemically upon mechanical stress and that, similarly to Ca^{2+}, the systemic response depends on the strength of the applied stimulus. The lack of systemic accumulation of L-glutamate in the leaves of 5- and ≥7-leaf-stage plants, where a Ca^{2+} increase was instead observed (Fig. 1C) might reflect limitations in iGluSnFR sensitivity or other physiological factors requiring further investigation. The use of the newly developed iGluSnFR indicators with improved activation kinetics, increased sensitivity, and tailored deactivation rates might be, therefore, considered in the future (*58*, *59*). Nevertheless, having established the feasibility of in planta imaging of apoplastic L-glutamate dynamics in *N. benthamiana* plants, we next assessed the response to a more natural condition, such as insect herbivory chewing. We therefore placed *S. littoralis* larvae onto the leaves of ≥7-leaf-stage *N. benthamiana* iGluSnFR plants, whose chewing triggered a localized increase in apoplastic L-glutamate. No corresponding increase was observed in systemic tissues (movie S7).

In conclusion, by combining the generation of *N. benthamiana* iGluSnFR plants with the MAPPI system, we extend the application of this technology beyond Ca^{2+} signaling to enable the in vivo study of leaf apoplastic L-glutamate dynamics. The obtained results suggest a conserved role for L-glutamate between *N. benthamiana* and *A. thaliana* (*32*, *34*, *53*).

From proof of concept to practical application of the MAPPI system: Real-time monitoring of cytosolic Ca^{2+} dynamics in plants under submergence as a case study

After demonstrating the functionality of the MAPPI system, we aimed to explore its broader potential by investigating environmental challenges commonly faced by plants. Among these, climate change presents significant risks, with submergence identified as a major threat to global agricultural productivity and food security (Food and Agriculture Organization of the United Nations, 2007) (*60*). Recent research has shown that *A. thaliana* seedlings subjected to flooding experience a cytosolic Ca^{2+} increase in root tips and that the absence of the cation exchanger 2 vacuolar transporter (which pumps Ca^{2+} into vacuoles) results in stronger and more prolonged Ca^{2+} signals (*61*). Additionally, Mittler's lab demonstrated that waterlogging of 4-week-old *A. thaliana* plants grown in peat moss induces systemic ROS and Ca^{2+} waves in the shoot (*62*). Building on these findings, we used the MAPPI system to perform real-time monitoring of Ca^{2+} dynamics in 5-leaf-stage *N. benthamiana* plants subjected to submergence (Fig. 3A). Plants were grown in soil in standard 5-cm pots, which were transferred into transparent

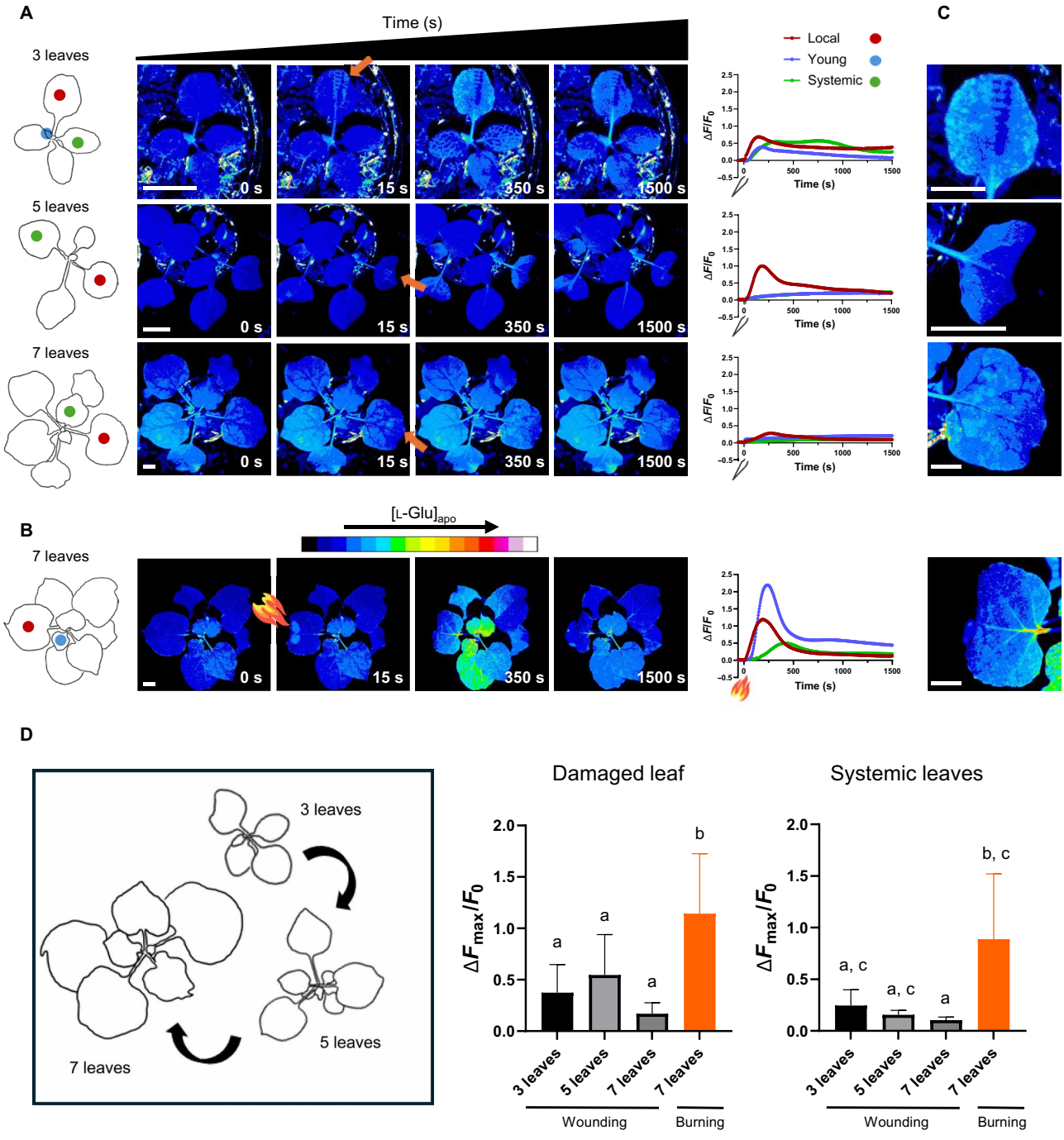

Fig. 2. Apoplastic L-glutamate levels in local and systemic leaves of iGluSnFR *N. benthamiana* plants in response to press wounding and leaf burning. (**A**) Left: Schematic representation of plants at different developmental stages used in the experiment. Colored dots indicate the leaves where iGluSnFR fluorescence was quantified: damaged leaves (red), young leaves (blue), and systemic leaves (green). Center: Representative false-color images (16-color lookup table) of plants before and after wounding. Scale bars, 1 cm. Arrows indicate the wounded leaf. Right: Normalized iGluSnFR fluorescence signals ($\Delta F/F_0$) over time from leaves of one representative plant for each developmental stage (3-, 5-, and ≥7-leaf stage). (**B**) Left: Schematic representation of plants at the selected developmental stage used in the experiment (≥7-leaf stage). Colored dots indicate the leaves where iGluSnFR fluorescence was quantified. Center: Representative false-color images (16-color lookup table) of plants, before and after burning. Scale bar, 1 cm. The flame indicates the burned leaf. Right: Normalized iGluSnFR fluorescence signals ($\Delta F/F_0$) over time of leaves of one representative plant for the selected developmental stage. (**C**) Enlargements of the damaged leaves in wounding (top) and burning (bottom). Enlargements of the sample at 350 s for all the developmental stages. Scale bars, 0.5 cm (3-leaf-stage sample) and 1 cm (all the other leaf stages). (**D**) Left: Schematic representation of plants at different developmental stages used in the analysis. Right: Maximal peak of normalized iGluSnFR fluorescence changes ($\Delta F_{max}/F_0$) in the local (left box) and systemic (right box) leaves after wounding or burning. Error bars, SD. For each chart, different letters indicate significant differences according to one-way ANOVA test ($P \leq 0.05$); $n \geq 3$ plants. Exposure time, 500 ms. Sampling interval, 5 s. Total acquisition time, 30 min. Wounding and burning were applied 3 min after the acquisition started.

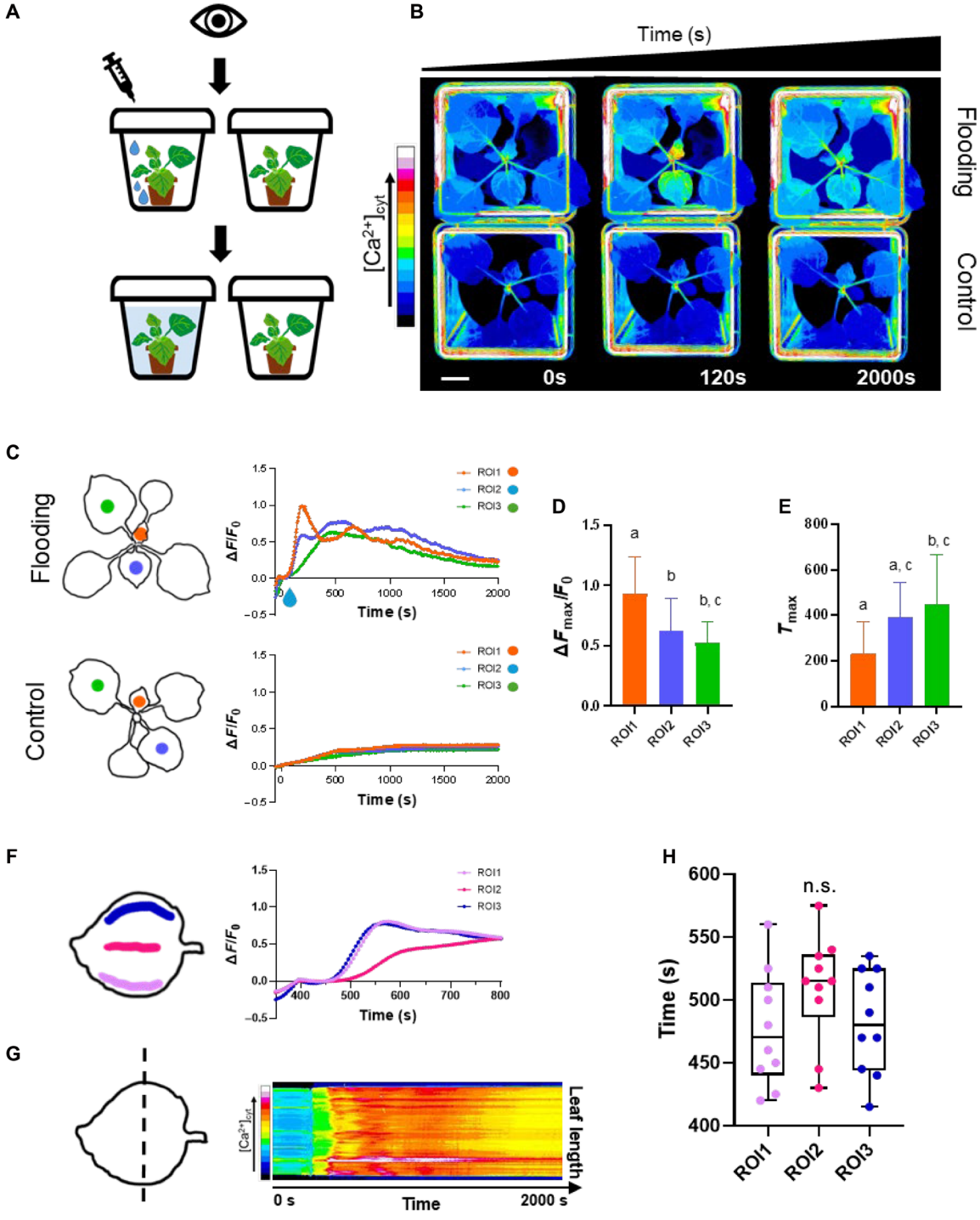

Fig. 3. Submergence of *N. benthamiana* plants triggers a rapid increase in cytosolic Ca^{2+} levels in leaf cells. (**A**) Schematic of the submergence experiment: Treated and control plants were imaged simultaneously using the vertical arm of the MAPPI setup. (**B**) Representative false-color images (16-color lookup table) of 5-leaf-stage plants expressing GCaMP3 before and after submergence. At each time point, a submerged plant (top) and a nonsubmerged control (bottom) are shown. Scale bar, 1 cm. (**C**) Left: Schematic of plants used in (B). Colored dots indicate quantified leaves: ROI1 (orange), ROI2 (blue), and ROI3 (green). Right: Normalized GCaMP3 fluorescence signals ($\Delta F/F_0$) from the indicated ROIs. (**D**) Maximal normalized GCaMP3 fluorescence change ($\Delta F_{max}/F_0$) in ROI1, ROI2, and ROI3 after submergence. (**E**) Time to maximum normalized signal (T_{max}) in the three ROIs. Error bars, SD; different letters denote significant differences (one-way ANOVA, $P \leq 0.05$); $n = 10$ plants. Exposure time, 500 ms. Sampling interval, 5 s. Total acquisition time, 35 min. Submergence was applied 3 min after the acquisition started. (**F**) Left: Schematic of the leaf marked with the blue dot (ROI2) in (C). Colored lines indicate the areas where GCaMP3 fluorescence was quantified: ROI1 (lilac), ROI2 (pink), and ROI3 (dark blue). Right: Normalized $\Delta F/F_0$ signals from these areas. (**G**) Left: Schematic of the same leaf showing the line used to build the kymograph. Right: Kymograph showing temporal intensity changes along this line. (**H**) Bar chart showing the time to reach 10% of the maximum signal in the ROIs shown in (F). n.s., not significant (one-way ANOVA); $n = 10$ plants.

plastic boxes (Magenta box) for submergence treatment (Fig. 3B). The pots were secured at the bottom of the Magenta boxes to prevent flotation, and a 3D printed black mask was used to contain soil and prevent leakage during submergence (fig. S2E). The large FOV of the MAPPI system allowed simultaneous imaging of two independent Magenta boxes, enabling one plant to be submerged, while the other served as an untreated control (Fig. 3, A and B). We acquired images every 5 s for 35 min. Three min after the start of the acquisition, 300 ml of water was added to one box to submerge the treated plant (Fig. 3B and movie S8). Although the addition of water temporarily affected background fluorescence, it did not obscure the detection of a steep increase in GCaMP3 fluorescence in various leaves (Fig. 3B and movie S8). This indicates that submergence induces a rapid cytosolic Ca^{2+} increase in leaves of soil-grown plants (Fig. 3, B and C, and fig. S8A). By plotting normalized GCaMP3 fluorescence changes over time for three different leaves differing in developmental stage (young, intermediate, and mature), we observed that younger leaves responded faster than older, larger leaves (Fig. 3, C to E). Notably, the analysis of the recorded time lapses revealed that the fluorescence change increases faster at the leaf margins compared to the main vasculature (Fig. 3, F to H, and movie S8). In the untreated control, a small increase in GCaMP3 fluorescence was detected in all analyzed leaves, which remained stable over the duration of the experiment (Fig. 3, B and C, and fig. S8B). Nonetheless, the distinction between the treated and untreated samples was evident. The ability to simultaneously image side by side the treated and control plants provided an invaluable experimental control.

An interesting observation was the higher and faster and more pronounced Ca^{2+} increase in younger leaves compared to that in older ones (Fig. 3, D and E). These different responses may be associated with the higher metabolic activity of young leaves. It has been shown that *A. thaliana* plants regulate the speed and pattern of leaf senescence during flooding by modulating the activity of the age-dependent ORESARA1 (ORE1). This mechanism ensures that older, expendable leaves are dismantled first, prolonging the survival of younger leaves and meristematic tissues vital for whole-plant survival (*63*). Our observations, thus, suggest that younger leaves may trigger a more efficient response, modulated by Ca^{2+} signaling, compared to older leaves. The ability to monitor in real time the response of different aged leaves offers a future opportunity to perform a wide array of molecular analyses such as transcriptomics, proteomics, and phosphoproteomics analyses in leaves, correlating molecular signatures with the magnitude at timing of the Ca^{2+} response.

Overall, this experiment illustrates the utility of MAPPI for dissecting age-dependent signaling responses to abiotic stress and paves the way for integrative studies linking Ca^{2+} dynamics to molecular reprogramming during submergence.

From one-side to two-side fluorescence imaging: Development of an orthogonal configuration of MAPPI system

The MAPPI system can be efficiently used for in planta Ca^{2+} imaging, leveraging its large FOV to address relevant biological questions (i.e., submergence). Having validated the single-view MAPPI system in key experiments (such as long-distance signaling and submergence response), we saw an opportunity to further enhance the setup. The vertical design allowed space for an additional horizontal arm mounted at a 90° angle, enabling simultaneous orthogonal imaging. We therefore upgraded MAPPI to a dual-view configuration (Fig. 4A), designed to capture complementary information, including side views of stems, roots, and leaf movements, which are not accessible from a single perspective.

To test this concept, we built a horizontal imaging arm identical to the original one, equipped with an independent illumination source and a second camera, and integrated it into the platform (Fig. 4A). The second arm was positioned at an appropriate distance from the vertical arm and at a height sufficient to place the sample at the intersection of the two optical axes. This ensured that the sample was in the illumination plane with maximal uniformity and centered in the FOV of both cameras. To enable synchronized illumination and data acquisition from both arms, we developed a custom Python-based software (see Materials and Methods). To validate the functionality of the orthogonal setup, we imaged at first ≥7-leaf-stage *N. benthamiana* plants expressing the GCaMP3 Ca^{2+} indicator (Fig. 4B and movie S9). For both views, we used the same exposure (i.e., 500 ms) and sampling times (5 s). As a proof of concept to test the functionality of the orthogonal setup, we challenged *N. benthamiana* plants with wounding and burning, following our previously established protocols (Fig. 1). Analysis of images acquired using the vertical arm camera confirmed earlier findings: In the case of wounding, the cytosolic Ca^{2+} increase was restricted to the wounded area, whereas leaf burning induced a Ca^{2+} wave that propagated to systemic leaves (Fig. 4B and movie S9). In contrast, the horizontal view provided additional insights, revealing Ca^{2+} wave propagation through the petiole and stem in burned plants (Fig. 4B and movie S9). The side view also captured leaf movement dynamics (movie S9): Burned leaves exhibited rapid and pronounced turgor loss, while wounded leaves showed only minor reductions, emphasizing the stronger physiological stress imposed by burning. A key strength of the upgraded MAPPI configuration is its ability to visualize leaf movement in parallel with Ca^{2+} imaging, thereby enabling previously unexplored experimental paradigms. To explore this further, we investigated whether nyctinasty leaf movements generate Ca^{2+} signals or propagate waves (Fig. 4C and movie S10). To test this hypothesis, we imaged 5-leaf-stage *N. benthamiana* GCaMP3 plants every 2.5 min for 16 hours (Fig. 4C). Analysis of the recorded movies (movie S10) revealed clear leaves movements consistent with a nyctinasty response (Fig. 4, C, F, and G) (*64*). However, these movements were not associated with detectable increase of cytosolic Ca^{2+} neither in the leaves (Fig. 4D), in the leaf petiole (Fig. 4E), nor in the region showing the maximum bending [region of interest 4 (ROI4) in Fig. 4 (F to H) and movie S10]. Together, our results demonstrate that MAPPI's orthogonal configuration enables simultaneous monitoring of morphological and biochemical dynamics, offering a powerful approach to dissect complex, stimulus-dependent relationships between plant movement and intracellular signaling.

MAPPI orthogonal configuration enables the visualization of a shoot-to-root Ca^{2+} wave propagation in *N. benthamiana* soil grown plants in response to leaf burning

The MAPPI system's unique capability to provide orthogonal imaging inspired us to investigate whether long-distance Ca^{2+} waves propagate not only between leaves but also from shoot-to-root. To explore this hypothesis, we aimed to monitor roots under natural growth conditions in soil. For this purpose, we developed a custom 3D printed rhizobox (a transparent-sided soil container to visualize

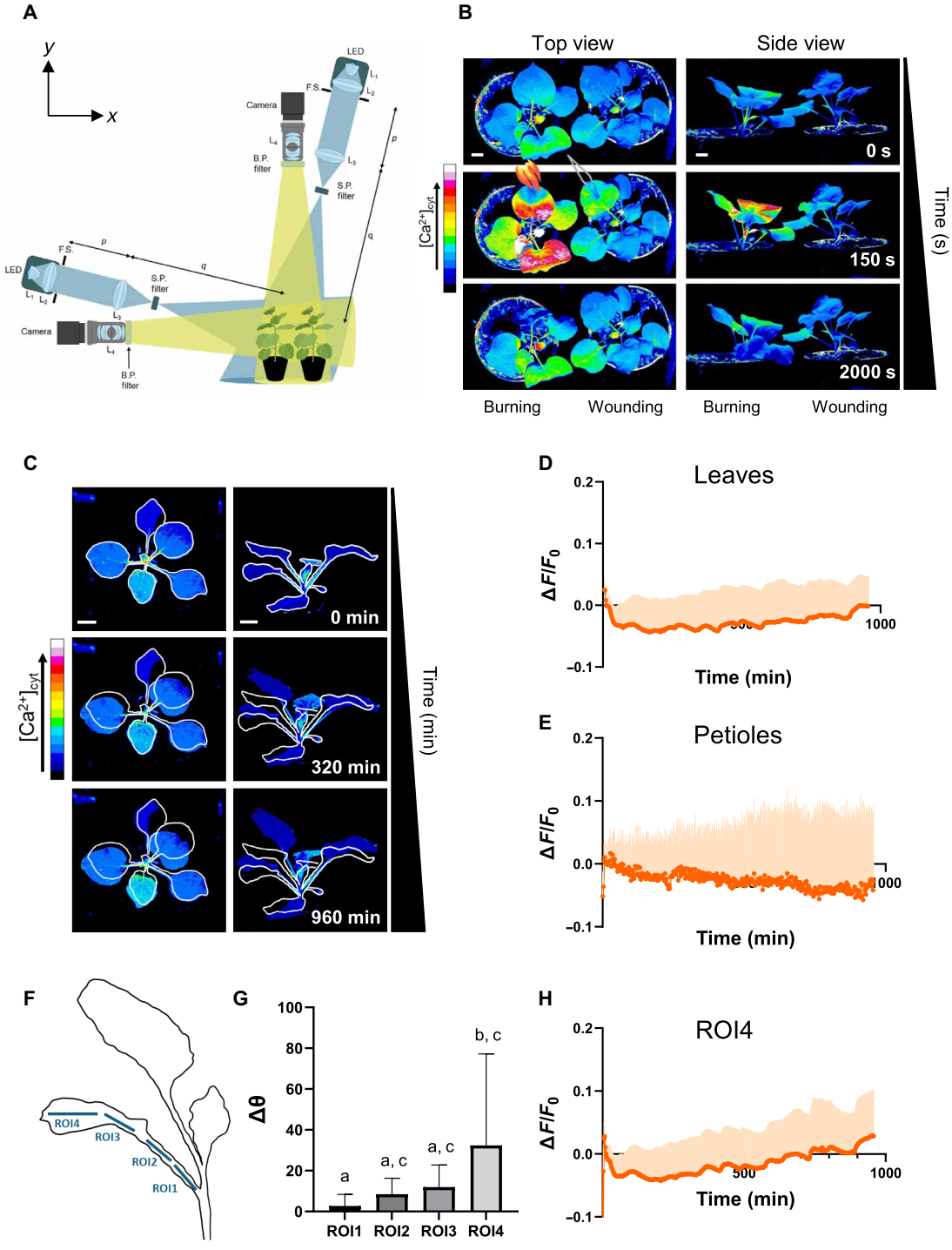

Fig. 4. Simultaneous orthogonal imaging of adult and 5-leaf-stage GCaMP3 *N. benthamiana* plants in response to wounding and burning or under overnight pulsed blue LED light illumination, respectively. (**A**) Scheme of the two arms MAPPI system. (**B**) False-color image (16-color lookup table) of two representative adult *N. benthamiana* plants expressing the GCaMP3 Ca^{2+} indicator before and after application of burning (left) and press wounding (right), respectively. Exposure time, 500 ms. Sampling time, 5 s. Acquisition time, 35 min. Stresses have been applied 3 min after the acquisition started. Scale bar, 1 cm. (**C**) False-color image (16-color lookup table) of one representative 5-leaf-stage *N. benthamiana* plant expressing the GCaMP3 Ca^{2+} indicator during overnight pulsed blue LED light illumination. The dual view allows to image nyctinasty leaves movements" with "This dual-view setup enables imaging of nyctinastic leaf movements. Exposure time, 500 ms. Sampling time, 2.5 min. Acquisition time, 16 hours. Scale bars, 1 cm. (**D** and **E**) Normalized GCaMP3 fluorescence signals ($\Delta F/F_0$) over time, from (D) leaves and (E) petioles. $n = 5$ plants. (**F**) Schematic representation of plant with the ROIs considered for petioles and leaf movement: ROI1 and ROI2 (petioles), and ROI3 and ROI4 (leaf). (**G**) Bar charts representing the variation in petiole and leaf angles during the 16-hour-long acquisition. (**H**) Normalized GCaMP3 fluorescence signals ($\Delta F/F_0$) over time for ROI4. Error bars, SD. Different letters indicate significant differences according to one-way ANOVA test ($P \leq 0.05$).

roots; fig. S2, A and B, and Fig. 5A). To prevent root growth into opaque soil regions, the rhizobox was designed with an oblique flange at its base, creating a 45° incline (fig. S2, A and B). This encouraged roots, responding to gravitropic stimuli, to grow toward the transparent plexiglass, providing clear visibility for fluorescence imaging. Figure 5 (A and B) shows 7-leaf-stage *N. benthamiana* GCaMP3 plants cultivated in the rhizobox, demonstrating that the MAPPI system's sensitivity is sufficient to detect GCaMP3 fluorescence in both leaves and roots (Fig. 5B). To test the hypothesis that Ca^{2+} waves travel from shoot-to-root, we applied a burning stimulus to a single leaf using a lighter and acquired images every 5 s with both MAPPI arms (Fig. 5B and movie S11). In addition to the expected cytosolic Ca^{2+} increase in systemic leaves, we repeatedly observed a Ca^{2+} rise in both primary and secondary roots (Fig. 5, B to D; fig. S9; and movie S11). GCaMP3 fluorescence changes were detected simultaneously along root zones (defined as ROIs spaced at 1-cm intervals). This likely reflects the fact that the current temporal resolution does not fully resolve the propagation dynamics of the wave (Fig. 5C). Nevertheless, it enabled the observation that the time to reach the maximum Ca^{2+} peak was shorter in the root tip (ROI5) than in the upper part of the root (ROI1) (Fig. 5, C to E). Moreover, the rhizobox's ability to accommodate two plants allowed a comparative analysis under identical growth conditions. Notably, the Ca^{2+} responses differed between the two plants. In plant N2, the signal clearly propagated, with intensity decreasing along the root. In contrast, plant N1 exhibited a considerably weaker response, even in the ROI closest to the shoot apparatus (ROI1; Fig. 5, C and D). This variability is plausibly explained by the lower overall Ca^{2+} increase in the damaged leaf of plant N1 compared to that of N2, supporting our earlier observations. The propagation of Ca^{2+} waves appears to depend on the intensity of the initial stimulus or the response of the injured leaf. Specifically, the $\Delta F_{max}/F_0$ GCaMP3 increase exceeded 2.5 in N2 but was below 2 in N1 (Fig. 5, C and D).

In summary, our results demonstrate that mechanical injury to a leaf can trigger cytosolic Ca^{2+} waves not only in systemic aerial tissues but also in the root system, under physiologically relevant conditions. Moreover, the extent of Ca^{2+} elevation in roots correlates with the strength of the local response in the damaged leaf, underscoring MAPPI's unique capability to capture integrated whole-plant signaling dynamics.

Motivated by having the possibility to monitor the Ca^{2+} dynamics in root and shoot in the same plant we then investigated whether the *S. littoralis* leaf chewing could lead to shoot-to-root Ca^{2+} wave propagation, using GCaMP3 *N. benthamiana* plants with a size that fits with the use of rhizotrons. As expected, the effect of larvae chewing triggered a significant cytosolic Ca^{2+} increase in the local chewed leaves, but when, with younger plants, it was able to chew the stem, the Ca^{2+} waves propagated to the roots (movies S12 and S13).

Salt stress treatment fails to induce a root-to-shoot Ca^{2+} wave propagation in *N. benthamiana* soil grown plants that is instead present in *A. thaliana*

To our knowledge, the first study reporting the existence of long-distance Ca^{2+} waves in plants was conducted by the Gilroy's lab study (*40*). This seminal work demonstrated that applying 100 mM NaCl to the root tip of 10-day-old *A. thaliana* seedlings induced a Ca^{2+} wave propagating to the shoot, leading to the up-regulation of stress marker gene expression (*40*). Similarly, Xiong and colleagues treated the roots of 7- to 8-week-old *A. thaliana* plants; transferred to tubes filled with water, with 200 mM NaCl; and observed the propagation of Ca^{2+} waves to the rosette leaves (*38*). Building on these findings, we sought to investigate whether, in mature plants grown in soil, salt stress sensing by the root could similarly trigger long-distance Ca^{2+} waves propagating to the shoot. To this end, we used the MAPPI system in combination with the custom 3D printed rhizobox (fig. S2, A and B) to visualize root-to-shoot Ca^{2+} signaling in soil-grown plants. To closely mimic natural conditions under which plants may encounter salt stress, we applied salt solution to the rhizobox base using a peristaltic pump, ensuring controlled perfusion at 3 ml/min (fig. S10A). This setup allowed localized treatment of the root under near-physiological conditions. To perform the experiment, *N. benthamiana* plants with five or more leaves, grown in rhizoboxes were watered weekly and the day before the experiment to maintain well-hydrated soil. Plants were then imaged for 3 min with both arms of the MAPPI system before initiating perfusion of either tap water (control) or tap water supplemented with 0.75 M NaCl (fig. S10E). As the solution filled the bottom reservoir (~10 ml), we observed a GCaMP3 fluorescence increase in the leaves after about 500 s, but no clear or reproducible response in the roots (fig. S10E and movie S14). However, by comparing the response to NaCl with the one observed with only water, there was no statistical difference with NaCl treatment (fig. S10E), suggesting that the Ca^{2+} increase in the leaves may depend either to an osmotic response, due to an increase in the soil water potential, or to the response to blue light rather than a specific salt-induced signal. To test the osmotic hypothesis, plants were watered 3 hours before the experiment to ensure soil water saturation, and the salt stress treatment was performed as described. Also, in this case, no significant differences were observed between water-only and NaCl treatments (fig. S10F). This result suggests that the GCaMP3 fluorescence increase, observed in the leaves, is possibly dependent on blue light, being of a magnitude like the small fluorescence increases reported in figs. S3F and S6E, and not due to water or salt treatment. We, thus, reasoned that, despite the high concentration of NaCl applied, dilution by the well-hydrated soil likely reduced the effective salt concentration to levels insufficient to induce a cytosolic Ca^{2+} increase in adult *N. benthamiana* plants. To address this, we increased the NaCl concentration to 1.5 M and compared plants watered the day before versus 3 hours before treatment (fig. S10, B to F). In the latter condition, only a subset of plants exhibited a cytosolic Ca^{2+} increase in the leaves (e.g., as shown by the peak in fig. S10F). These results suggest that, under near-physiological conditions, the NaCl concentrations used were insufficient to induce reliably the long-distance Ca^{2+} signals observed previously in young seedlings grown on plates (*38*). Nevertheless, several days after treatment, plants exposed to 1.5 M NaCl displayed clear stress symptoms (fig. S10G), indicating that the stress was perceived.

Given the limited Ca^{2+} response observed in *N. benthamiana*, we repeated the experiment with *A. thaliana* plants expressing GCaMP3 (Fig. 6A and movie S15) (*30*). Four-week-old plants, watered 3 hours before the experiment, were treated with 1 M NaCl (using the peristaltic pump), and, in contrast to *N. benthamiana*, *A. thaliana* plants showed a clear cytosolic Ca^{2+} increase both in shoots and roots (Fig. 6, A, C, and D; and movie S15), with distinct dynamics across different leaves (Fig. 6, A and C). Notably, in the roots, a propagation of the Ca^{2+} wave was evident (Fig. 6D) but highly variable, making it difficult to perform a statistical analysis of maximum Ca^{2+} amplitude

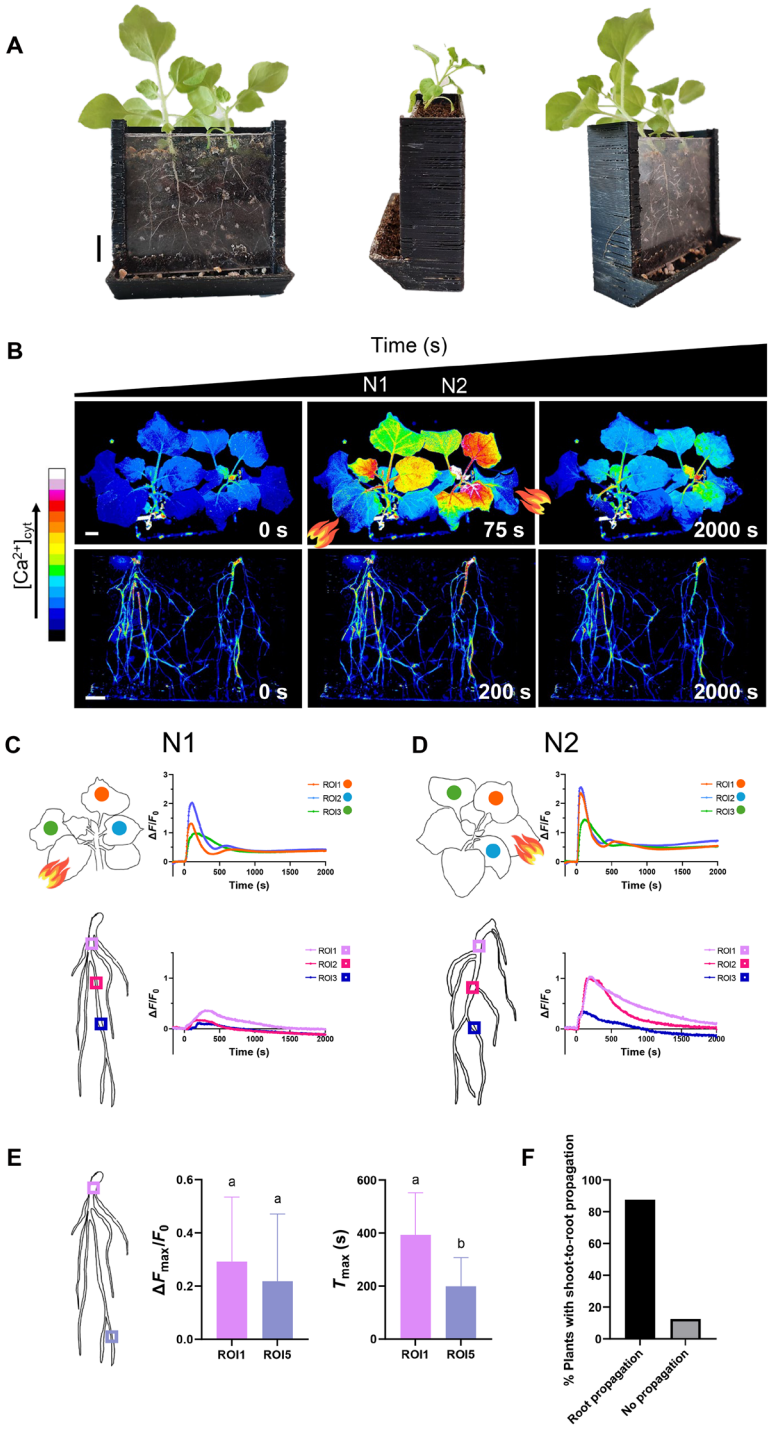

Fig. 5. Shoot-to-root Ca^{2+} signal propagation in ≥7-leaf-stage GCaMP3 *N. benthamiana* plants subjected to leaf burning. (**A**) Example of 3D printed rhizoboxes designed to perform dual-view experiments on *N. benthamiana* samples. (**B**) False-color images (16-color lookup table) of shoot and root of two representative pre-burn and after-burn ≥7-leaf-stage *N. benthamiana* plants expressing the GCaMP3 Ca^{2+} indicator. Flames indicate the burned leaves. Exposure time, 500 ms. Sampling time, 5 s. Acquisition time, 35 min. Leaf burning was applied 3 min after the acquisition started. Scale bars, 1 cm. (**C** and **D**) Left: Schematic representation of the shoot and the root of plants used in the experiment. Colored dots and squares indicate the leaves and the root areas where GCaMP3 fluorescence was quantified. Right: Normalized GCaMP3 fluorescence signals ($\Delta F/F_0$) over time from the ROIs selected in the shoot and the root of the two representative plants. (**E**) Left: Schematic representation of roots with the ROIs considered for the analysis (ROI1 and ROI5). Center: Maximal peak of normalized GCaMP3 fluorescence changes ($\Delta F_{max}/F_0$) in the considered ROIs. Right: Time to maximum normalized signal (T_{max}) in the considered ROIs. Error bars, SD. For each chart, different letters indicate significant differences according to *t* test ($P \leq 0.05$). (**F**) Percentage of plants where the shoot-to-root Ca^{2+} propagation was reported. $n = 8$ plants.

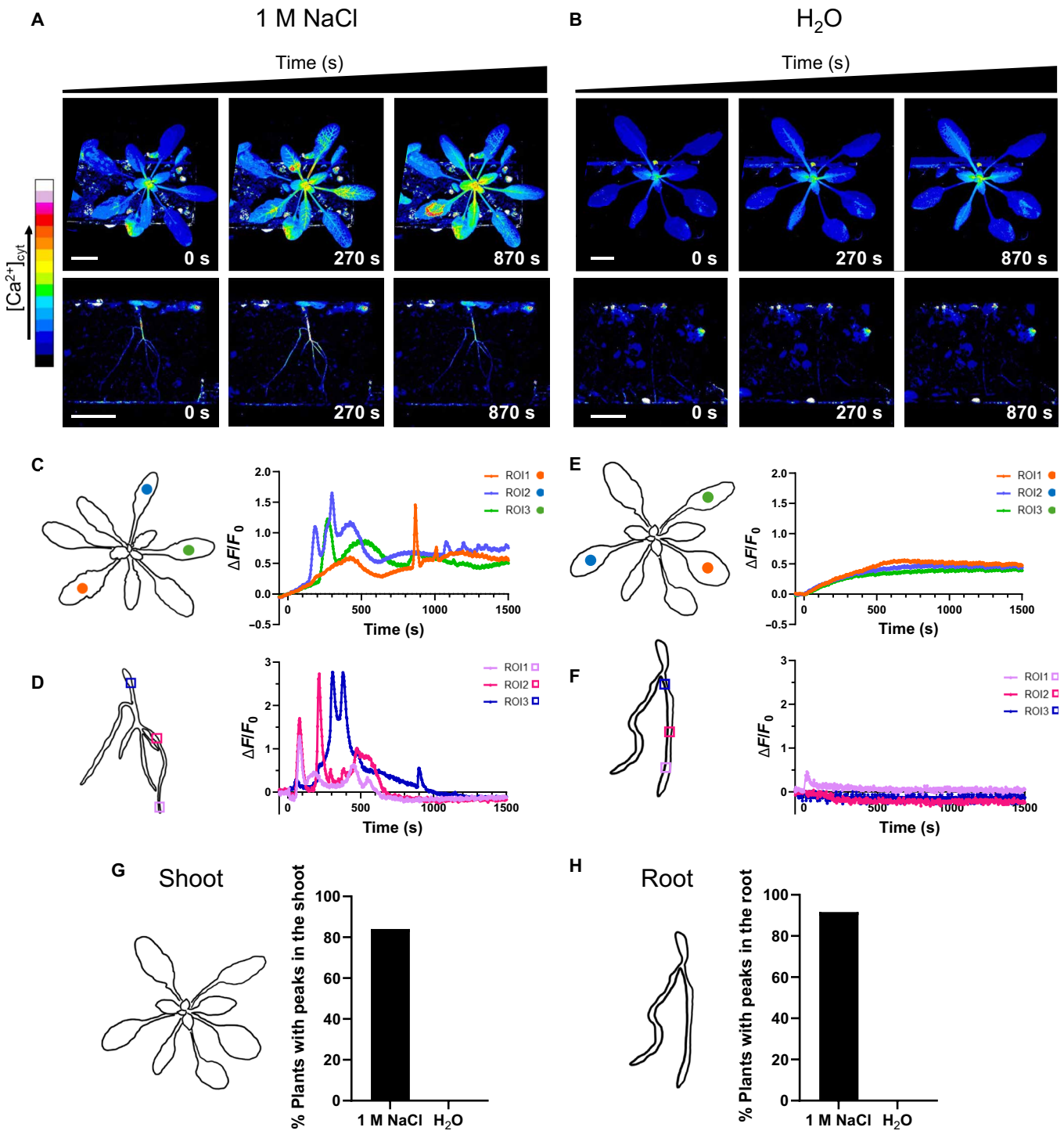

Fig. 6. Root-to-shoot Ca^{2+} signal propagation in adult samples of GCaMP3 *A. thaliana* treated with NaCl. (**A** and **B**) False-color images (16-color lookup table) of shoot and root of *A. thaliana* adult plants expressing the GCaMP3 Ca^{2+} indicator before and after (A) 1 M NaCl or (B) H_2O treatment. Scale bars, 1 cm. (**C** and **D**) Left: Schematic representation of the shoot and the root of plants used in the experiment. Colored dots and squares indicate the leaves and the root areas where GCaMP3 fluorescence was quantified. Right: Normalized GCaMP3 fluorescence signals ($\Delta F/F_0$) over time from the ROIs selected in the shoot and the root of one representative plant treated with 1 M NaCl. (**E** and **F**) Left: Schematic representation of the shoot and the root of plants used in the experiment. Colored dots indicate the leaves and the regions of the root where the three ROIs were analyzed. Right: Normalized GCaMP3 fluorescence signals ($\Delta F/F_0$) over time from the ROIs selected in the shoot and the root of one representative plant treated with H_2O (control). (**G**) Bar chart with the percentage of plants that showed Ca^{2+} peaks in the shoot. (**H**) Bar chart with the percentage of plants that showed Ca^{2+} peaks in the root. Exposure time, 500 ms. Sampling time, 3 s. Acquisition time, 30 min. Salt stress has been applied 3 min after the start of the acquisition. $n = 10$ plants for NaCl treatment, and $n = 6$ plants for H_2O treatment.

and timing of the peak response. Nonetheless, the response was observed in the shoot and in the root of 83.3 and 91.6% of plants, respectively (Fig. 6, G and H). Plants treated with water alone did only show a a modest increase in fluorescence in the leaves (Fig. 6, B, E, and F), which can again be attributed to the effect of blue light illumination. This increase did not cause confounding effects, as the fluorescence response to NaCl remained clearly distinguishable.

In conclusion, this series of experiments confirms that local salt sensing at the root level triggers long-distance Ca^{2+} waves propagating to the shoot in adult, soil-grown *A. thaliana*, but not in *N. benthamiana*. This difference could be attributed to a distinct sensitivity of the root systems to NaCl of the two different species, suggesting that the primary driver of the Ca^{2+} response may be a hyperosmotic stress rather than sodium toxicity (*65*).

Overall, our findings highlight species-specific differences in root-to-shoot Ca^{2+} signaling under salt stress. Using the MAPPI system, together with soil-grown rhizoboxes, was key to revealing these physiological differences under conditions that closely mimic the natural environment.

DISCUSSION

The development of the MAPPI platform enables fluorescence imaging across entire, soil-grown plants, overcoming key limitations of conventional microscopy. By providing a large FOV, modular dual-view geometry, and compatibility with genetically encoded intensiometric fluorescent indicators, MAPPI facilitates real-time visualization of dynamic physiological signals in whole plants under physiological conditions. This capability allows researchers to investigate systemic responses with spatial and temporal resolution that were previously difficult to achieve outside model systems (*66*, *67*).

Using MAPPI, we demonstrated that mechanical stress, such as leaf wounding and burning in *N. benthamiana*, triggers long-distance Ca^{2+} waves that propagate from the site of damage to distal leaves. These observations confirm that systemic Ca^{2+} signaling is not restricted to model species such as *A. thaliana* and support the idea that long-range Ca^{2+} responses are a conserved feature. The dependence of wave propagation on plant size suggests that developmental stage and morphological context influence signal transmission, which may reflect differences in vascular architecture, cellular competency, or tissue hydration. These findings underscore the importance of studying systemic signaling in intact, mature plants rather than relying solely on seedlings or young plants.

The observation that two halves of a single leaf can display temporally distinct responses to the same burning stimulus suggests that intraorgan signal propagation may be more complex than previously assumed. This asymmetry raises questions about the anatomy of signaling pathways within leaves, possibly reflecting differences in vascular connectivity or tissue damage thresholds. Such spatially heterogeneous responses highlight the value of wide-field imaging tools like MAPPI in capturing subtle yet biologically meaningful variation across tissue compartments.

The addition of an orthogonal imaging arm enabled simultaneous side- and top-view monitoring, allowing MAPPI to detect leaf movements associated with nyctinasty, revealing that they do not trigger Ca^{2+} signals. This dual-view geometry reveals plant behaviors that would be difficult to detect with a single top-down perspective and demonstrates MAPPI's utility in linking molecular and morphological dynamics in a single experimental setup.

Application of MAPPI to study long-distance Ca^{2+} signal in response to local application of salt stress revealed differences between *N. benthamiana* and *A. thaliana* plants. The absence of a reproducible root-to-shoot Ca^{2+} wave signal in *N. benthamiana* suggests a species-specific stress threshold. This difference may reflect variations in root architecture, or just sensitivity to salt stress, and supports the need to study stress responses in multiple species using platforms that preserve whole-plant context.

Last, using the L-glutamate biosensor iGluSnFR in *N. benthamiana* plants, we visualized leaf apoplastic L-glutamate dynamics in response to mechanical wounding, burning, and insect chewing. Our results, together with earlier observations in *A. thaliana* (*32*, *34*, *53*), point to a shared yet adaptable signaling function for L-glutamate in systemic wound response, modulated by both species and stimulus severity.

Despite these advances, some aspects of the system could benefit from further refinement. The temporal resolution of MAPPI, for example, could be enhanced by using more sensitive sensors or increasing illumination intensity. These modifications would enable the detection of fast transient signals and weakly expressed reporters, expanding the platform's utility for studying rapid or low intensity signaling events. However, such improvements involve trade-offs: Scientific CMOS cameras would raise the overall cost of the system, while higher LED or laser power could introduce photobleaching or plant physiological responses (*68*).

While the single-fluorophore indicators used in this study enabled reliable visualization of Ca^{2+} and L-glutamate dynamics across the whole plant, future adaptations of MAPPI could benefit from the use of FRET-based sensors (*6*, *33*). These ratiometric indicators allow internal signal normalization, reducing the impact of factors such as leaf curvature, tissue thickness, and light scattering. The implementation of FRET sensors would support more accurate quantification of signal amplitudes and dynamics, particularly when comparing responses across different organs, developmental stages, or treatments. Although this approach would also require increased system complexity, such as a dual-channel detection, it could further strengthen the capacity of MAPPI for precise analysis of systemic signaling, as well as enable the use of newly developed FRET-based sensors for in vivo studies of hormone dynamics, including for example: abscisic acid (ABA), gibberellins, and salicylic acid (*69*–*71*).

Broadening the scope of studies to include diverse genotypes, species, and environmental conditions will also be essential for evaluating the generality of the observed systemic responses and identifying species-specific regulatory features. Incorporating multiwavelength excitation and detection could further extend MAPPI's capabilities to support simultaneous imaging of different reporters, although this would likely increase both the system's complexity and physical size. Future applications of MAPPI could include imaging of hormone reporters, pathogen-triggered responses, or translocation of transcriptional regulators in real time.

Its compatibility with low-cost components and open-source control software makes MAPPI adaptable for use in diverse laboratory settings. To maximize its utility, community-driven improvements, such as enhanced temporal resolution, integration with light stimulation, or compatibility with multiparameter sensors, could extend MAPPI's relevance to both fundamental plant science and applied crop research.

MATERIALS AND METHODS

Plant materials and growth conditions

For the studies conducted in this research, *N. benthamiana* and *A. thaliana* plants expressing the GCaMP3 Ca^{2+} indicator under control of the *CaMV35S* promoter reported in (*29*) and (*30*), respectively, were used. Seeds were directly sown on the soil. Depending on the treatment, the plants were grown in 5-cm pots filled with Duemme technic soil or in 3D printed rhizoboxes (7.8 cm by 2.9 cm by 8 cm or 7.8 cm by 2.9 cm by 4 cm) filled with a 1:4 soil:perlite ratio. After 2-day stratification period at 4°C in the dark, the seeds were transferred to a growth chamber with controlled environmental conditions. Both *N. benthamiana* and *A. thaliana* plants were cultivated under long-day conditions (16-hour light–8-hour dark; 50 μmol of photons m^{-2} s^{-1} with Cool White Neon lamps), 50 to 60% relative humidity and temperatures of 22°C (light) and 18°C (dark). Imaging experiments were conducted on plants at different developmental stages: with two, three, five, and seven or more leaves for *N. benthamaiana* and on 5-week-old plants for *A. thaliana.*

Transformation of *N. benthamiana*

Transformation of *N. benthamiana* plants was performed through leaf disk transformation and organogenesis regeneration protocol (*72*). Seeds of wild-type *N. benthamiana* were surfaces sterilized with ethanol with the following steps: 10 min of 70% ethanol (EtOH), 1 min of 96% EtOH, and two washing with water. Seeds were then sown on solidified $^1/_2$ Murashige and Skoog (MS) medium (*73*) [$^1/_2$ MS salt, 1.5% sucrose, MES (0.5 g/liter), and agar (5 g/liter), pH 5.8] in Magenta box (Sigma-Aldrich) and kept in growing chamber at 24°C, long day, 16-hour light and 8-hour dark.

Two days before the transformation, *Agrobacterium tumefaciens* LBA4404 strain carrying the pBIN42-35S-CHIB-iGluSnFR construct was plated on solid LB medium and grown overnight at 28°C. The following day, the liquid culture was prepared, starting from a single colony bacteria grew on plate, with 50 ml of liquid yeast extract peptone medium [yeast extract (10 g/liter), peptone (10 g/liter), and NaCl (5 g/liter), pH 7.0], supplemented with rifampicin (25 μg/ml), streptomycin (50 μg/ml), and kanamycin (50 μg/ml), and grown with a 180 rpm shaking at 28°C.

On the day of the transformation, the bacterial culture was pelleted and resuspended in 25 ml of MS medium (full MS salt and 3% sucrose, pH 5.8, with a final optical density at 600 nm of 0.5) with 200 μM acetosyringone. Leaf explants were maintained in bacterial suspension for 10 to 15 min. After the incubation, leaf explants were washed with fresh MS medium, dried on sterile paper, and maintained in petri dishes containing MSIB medium [full MS salt, 3% sucrose, MES (0.5 g/liter), plant agar (5 g/liter), indole-3-butyric acid (IBA) (1 mg/liter), and 6-benzylaminopurine (6-BAP) (1 mg/liter), pH 5.8] in the dark for 48 hours. Two days posttransformation, leaf explants were transferred to freshly prepared MSIB petri dish plates supplemented with cefotaxime (200 mg/liter), carbenicillin (200 mg/liter), and kanamycin (50 mg/liter) and maintained in the growing chamber. Every 2 weeks, leaf explants were transferred on fresh MSIB until shoot organogenesis. Regenerants were transferred on $^1/_2$ MS medium supplemented with cefotaxime, carbenicillin, and kanamycin for rooting. We selected 13 independent lines, and we used one transgenic line (line 2) for all experiments.

Confocal laser scanning microscopy

Confocal microscopy analyses of stable *N. benthamiana* plants expressing GCaMP3 and iGluSnFR indicators were performed using a Nikon Eclipse Ni-U upright microscope, equipped with a Nikon A1 laser scanning device (www.nikon.com/). For localization studies, samples of *N. benthamiana* GCaMP3 and iGluSnFR leaves were incubated in a solution of propidium iodide (20 μg/ml; PI) for 20 min before acquisition. Images were acquired by a CFI Apo LWD Lambda S 40XC WI (numerical aperture, 1.15). GCaMP3 and iGluSnFR were excited with the 488-nm laser, and the emission was collected at 505 to 550 nm. PI was excited with the 561-nm laser, and the emission was collected at 570 to 620 nm. The confocal pinhole was set to 17.9 μm, and the images were acquired at 2048 × 2048 pixel resolution. NIS-Elements (Nikon; www.microscope.healthcare.nikon.com/it_EU/products/software/nis-elements/software-resources) was used as a platform to control the microscope. Images in fig. S5 were denoised by using the NIS-Elements Denoise.ai plugin (www.microscope.healthcare.nikon.com/en_EU/products/confocal-microscopes/a1hd25-a1rhd25/nis-elements-ai).

Stereomicroscope fluorescence microscopy

Two-leaf-stage *N. benthamiana* GCaMP3 plants were imaged with a Nikon stereomicroscope (SMZ18, www.nikon.com/) equipped with an ORCA-Fusion BT sCMOS camera (www.hamamatsu.com/eu/en/product/cameras/cmos-cameras/C11440-42U40.html). Excitation light (460 nm) was produced by a CoolLED pE-300ultra (www.coolled.com/) with a green fluorescent protein (GFP) filter cube. A Plan Apo 0.5× objective was used, and images were collected with an exposure time of 500 ms with a 4 × 4 camera binning (1440 × 1024 pixels). GCaMP3 images were acquired every 5 s with the GFP filter cube.

3D printed chambers and equipment

To perform shoot-to-root and root-to-shoot experiments, we designed and built custom 3D printed rhizoboxes. The design process was carried out using Fusion 360 CAD software (Autodesk, www.autodesk.com/), and the resulting 3D models were exported in STL format. These files were processed using UltiMaker Cura, an open-source slicing software (https://ultimaker.com/software/ultimaker-cura) and printed with a Kobra 3D printer (Anycubic, https://store.anycubic.com/products/kobra) at 0.2-mm resolution using polylactic acid (PLA) filament. Each rhizobox consisted of three opaque black PLA walls and one transparent wall made of either glass or plexiglass, tightly fitted to ensure stability. To promote root growth along the transparent surface, rhizoboxes were positioned at a 45° angle during plant growth. For subirrigation during both normal growth and salt treatments, each rhizobox was paired with a custom 3D printed plant saucer (fig. S2, A and B). To avoid double illumination of the shoot during image acquisition using two orthogonal cameras, a partition was also 3D printed (fig. S2C). This partition featured an inclined plane supported by two telescopic legs, allowing it to adapt to different rhizobox sizes. Leaf wounding in *N. benthamiana* was performed using flat-tipped, 3D printed tweezers of varying sizes, selected on the basis of the developmental stage of the plant (fig. S2D). For submergence experiments, we printed a base that secured the plants at the bottom of the Magenta box to prevent floating (fig. S2E). Additionally, a 3D printed black mask, matching the pot diameter, was used to prevent soil from spilling out during water submersion (fig. S2E).

Multiview imaging system

The implemented imaging setup consists of two identical arms positioned at 90° relative to each other, enabling fluorescence imaging of

the sample both vertically and horizontally. In each arm, excitation light is provided by a high-power LED centered at 470 nm (SOLIS-470C- High-Power LED for Microscopy, Thorlabs) and equipped with four emitters allowing for enhanced power compared to standard LEDs. A system of two lenses, integrated within the LED, creates a homogeneous illumination plane at the field stop plane located right outside of the LED cage. Here, a diaphragm is placed to control the size of the final illumination field at the sample. A third lens (with focal length $f = 75$ mm), positioned at a distance greater than its focal length from the field stop (distance from the lens $p = 90$ mm), is used to conjugate the field stop with the sample to maximize illumination uniformity and obtain an enlarged image of the illumination plane at the sample (the distance between the third lens and the sample plane with maximized uniformity is fixed and was calculated using the thin lens equation; with the chosen f and p, it is equal to $q = 450$ mm). With the diaphragm fully open, an illumination field of 20 cm in diameter is achieved on the sample. A short-pass filter at 500 nm (FESH0500, Thorlabs) is placed at the aperture stop to ensure proper selection of the excitation light. No diaphragm is used at this point of the optical path as the intensity of the excitation beam can be effectively modulated via the LED dimmer. The detection unit comprises a macro-objective for Machine Vision (MVL16M1, Thorlabs), preceded by a band-pass filter centered at 542 nm (BrightLine 542/27-50, Semrock), and a CMOS camera (GS3-U3-23S6M-C, FLIR Grasshopper). The objective offers a 46° FOV used in combination with a 1/1.2 inch (13.33 mm) sensor like the one of the implemented camera. Both vertical and horizontal arms are mounted on rails, allowing easy adjustment of the distance between the single-arm setup and the sample. This flexibility is essential, as the imaging system is designed to accommodate plant samples of varying sizes. However, while moving the illumination unit, it must be considered that the distance between the third lens and the sample plane with maximized illumination uniformity is fixed and is equal to the calculated q value. A table with all the components necessary to build the MAPPI platform and precise instructions to reproduce the setup is provided on the dedicated GitHub repository (https://github.com/micropolimi/MAPPI).

Acquisition software

The MAPPI system is controlled by a Python-based ScopeFoundry open-source software available on GitHub (https://github.com/micropolimi/MAPPI). Each LED switch-on is modulated via an external TTL signal managed by an integrated circuit (DLP-IO8-G, DigiKey) and synchronized with the camera acquisition, allowing to reduce the amount of unnecessary light shined on the sample while not acquiring data. For each acquisition cycle, the LED illumination was activated 250 to 500 ms before image capture to allow the LED light output to reach a stable level before exposure. Images were acquired using a 500-ms exposure time and 3- or 5-s sampling intervals. This acquisition protocol represents a balanced compromise between temporal resolution, signal integrity, and minimal photonic load on the sample, ensuring accurate representation of the Ca^{2+} dynamics while limiting plant photostimulation. The software coordinates the two-arm acquisition process, ensuring synchronization between both arms. Data from both arms are stored by the acquisition software in a single HDF5.

MAPPI imaging of adult soil grown plants

Imaging of *N. benthamiana* and *A. thaliana* plants using the MAPPI system was conducted by exciting the samples with the 470-nm LEDs light with an exposure time of 500 ms and collecting the emission at 542/27 nm. Images were acquired every 5 and 3 s for *N. benthamiana* and *A. thaliana*, respectively. Depending on the experiment, either only the vertical arm or both the vertical and the horizontal arms were used (table S1). When both imaging units were used, the acquisition parameters were set identical for both arms. Unless otherwise specified, treatments were applied 3 min after the start of image acquisition.

Leaf wounding and burning

Wounding treatments were applied on *N. benthamiana* plants at different developmental stages: two, three, five, and seven or more leaves. The 2-leaf-stage plants were imaged using both a stereo microscope and the MAPPI system, while older *N. benthamiana* plants were imaged exclusively with the MAPPI system. In both cases, images were acquired every 5 s over a 35-min acquisition, with exposure time of 500 ms for both the stereomicroscope and the MAPPI system. Wounding treatment was performed 3 min after the start of the acquisition. Burning experiments were performed with the MAPPI using ≥7-leaf-stage plants for leaf-to-leaf and shoot-to-root Ca^{2+} propagation. Images were acquired every 5 s over a 35-min acquisition, with 500-ms exposure time. Burning was applied 3 min after the start of the acquisition. In shoot-to-root experiments, both the x- and y-axis arms were used, and both the LEDs were activated to illuminate the shoot and the root apparatuses. To avoid double illumination of the shoot, a 3D printed mask was located in between the sample and the x-axis LED.

Nyctinasty leaf movements

Nyctinasty leaf movement experiments were conducted using *N. benthamiana* plants with five or more leaves. The samples were placed under the MAPPI system and imaged every 2.5 min over a 16-hour period, with and exposure time of 500 ms. Both vertical and horizontal arms were used, but only the y-axis LED was activated.

NaCl treatment

Salt stress treatments were applied to five- or more-leaf-stage *N. benthamiana* and 5-week-old *A. thaliana* plants grown in soil within customized 3D printed rhizoboxes. *N. benthamiana* and *A. thaliana* plants were imaged every 5 and 3 s, respectively, over a 35-min acquisition time for tobacco and a 30-min acquisition time for *A. thaliana*, with an exposure time of 500 ms. Both the x- and y-axis arms were used, and a 3D printed mask was placed to prevent double illumination of the shoot. Solutions began flowing into the bottom of the rhizobox chamber 3 min after the start of the acquisition. Tap water and NaCl solutions were delivered to the bottom of the box via a perfusion system using a peristaltic pump (Masterflex Isamtec), ensuring a constant flow rate of 3.3 ml/min. *N. benthamiana* plants were treated with tap water, 0.75 M NaCl, and 1.5 M NaCl solutions while *A. thaliana* with tap water and 1 M NaCl solution. This system allows filling only the chamber reservoir (~10 ml) with the solution.

Submergence experiments

Submergence experiments were conducted using 5-leaf-stage *N. benthamiana* plants grown in 5-cm pots. The plants were placed in Magenta boxes and fixed to the bottom with a 3D printed hook to avoid floating (fig. S2E). To prevent soil leakage, a 3D printed black

mask was positioned at the top of the pot. Images were acquired every 5 s for a 35-min acquisition time, with 500-ms exposure time, using only the *y*-axis arm. Distilled water was added to the Magenta box from 3 min after the start of the acquisition with a syringe positioned in one corner of the box to avoid direct watering of individual leaves. Around 300 ml of distilled water was added paying attention to completely submerge the plant.

Image analysis with Fiji

HDF5 files were exported to Fiji, where images belonging to the two different channels of the double-view system were separated and analyzed individually. If there was no significant movement of the sample during the acquisition, then fluorescence intensity was extracted from the images using the basic features of Fiji. Custom-made ROIs were drawn on one frame of the time-lapse dataset, and the mean intensity value of the pixels inside each ROI was extracted and exported to an Excel workbook where $\Delta F/F_0$ was calculated. In every dataset, a ROI for removal of background was selected. Per each time point, background was subtracted from the intensity value of the ROIs before calculating the $\Delta F/F_0$. For flooding and dual-view burning experiments, a Savitzky-Golay filter was applied to the calculated $\Delta F/F_0$ before identifying the maximal peak of normalized GCaMP3 fluorescence changes ($\Delta F_{max}/F_0$), the time to the maximum normalized signal (T_{max}), and the time to reach 10% of the maximum peak.

Kymographs were generated using the KymographBuilder plugin by Fiji by drawing a straight line that crosses the leaf from one side to the other allowing visualization of spatial and temporal dynamics of fluorescence signals.

Image registration

In case of sample movement and growth, quick and efficient extraction of intensity information becomes difficult, requiring data registration. To address this need, we developed the napari-roi-registration plugin for napari, an open-source platform for visualization and analysis of multidimensional images in Python. The main feature of the plugin is provided by the Registration Widget and consists in allowing for the simultaneous registration of a nonlimited number of ROIs. The user selects the ROIs in a single frame of the dataset, and the plugin automatically identifies these regions across all images in the stack. The registration process relies on the Enhanced Correlation Coefficient image alignment algorithm implemented through the OpenCV Python library. Once the ROIs are identified, extraction of ROIs intensities and displacement is possible through the Processing Widget. After this, the analysis pipeline is the same used for intensity extracted using Fiji tools.

By using the napari-roi-registration plugin, we were able to follow the selected ROIs across multiple frames, achieving precise and efficient intensity extraction. The software is open-source and available on GitHub (https://github.com/GiorgiaTortora/napari-roi-registration) and the napari-hub (www.napari-hub.org/plugins/napari-roi-registration).

Supplementary Materials

The PDF file includes:
Figs. S1 to S10
Table S1
Legends for movies S1 to S15

Other Supplementary Material for this manuscript includes the following:
Movies S1 to S15

REFERENCES

1. A. Walia, R. Waadt, A. M. Jones, Genetically encoded biosensors in plants: Pathways to discovery. *Annu. Rev. Plant Biol.* **69**, 497–524 (2018).
2. F. L. Wang, Y. L. Tan, L. Wallrad, X. Q. Du, A. Eickelkamp, Z. F. Wang, G. F. He, F. Rehms, Z. Li, J. P. Han, I. Schmitz-Thom, W. H. Wu, J. Kudla, Y. Wang, A potassium-sensing niche in *Arabidopsis* roots orchestrates signaling and adaptation responses to maintain nutrient homeostasis. *Dev. Cell* **56**, 781–794.e6 (2021).
3. R. Waadt, J. Kudla, H. Kollist, Multiparameter in vivo imaging in plants using genetically encoded fluorescent indicator multiplexing. *Plant Physiol.* **187**, 537–549 (2021).
4. J. H. Rowe, M. Josse, B. Tang, A. M. Jones, Quantifying plant biology with fluorescent biosensors. *Annu. Rev. Plant Biol.* **76**, 285–315 (2025).
5. Y. Fichman, R. Mittler, A systemic whole-plant change in redox levels accompanies the rapid systemic response to wounding. *Plant Physiol.* **186**, 4–8 (2021).
6. M. Grenzi, F. Resentini, S. Vanneste, M. Zottini, A. Bassi, A. Costa, Illuminating the hidden world of calcium ions in plants with a universe of indicators. *Plant Physiol.* **187**, 550–571 (2021).
7. S. Buratti, M. Grenzi, G. Tortora, S. P. Nastasi, E. Dell'Aglio, A. Bassi, A. Costa, Noninvasive *in planta* live measurements of H_2O_2 and glutathione redox potential with fluorescent roGFPs-Based sensors. *Methods Mol. Biol.* **2798**, 45–64 (2024).
8. M. J. Berridge, P. Lipp, M. D. Bootman, The versatility and universality of calcium signalling. *Nat. Rev. Mol. Cell Biol.* **1**, 11–21 (2000).
9. E. Carafoli, J. Krebs, Why calcium? How calcium became the best communicator. *J. Biol. Chem.* **291**, 20849–20857 (2016).
10. P. J. White, M. R. Broadley, Calcium in plants. *Ann. Bot.* **92**, 487–511 (2003).
11. J. Kudla, O. Batistic, K. Hashimoto, Calcium signals: The lead currency of plant information processing. *Plant Cell* **22**, 541–563 (2010).
12. K. H. Edel, E. Marchadier, C. Brownlee, J. Kudla, A. M. Hetherington, The evolution of calcium-based signalling in plants. *Curr. Biol.* **27**, R667–R679 (2017).
13. J. Kudla, D. Becker, E. Grill, R. Hedrich, M. Hippler, U. Kummer, M. Parniske, T. Romeis, K. Schumacher, Advances and current challenges in calcium signaling. *New Phytol.* **218**, 414–431 (2018).
14. M. R. McAinsh, J. K. Pittman, Shaping the calcium signature. *New Phytol.* **181**, 275–294 (2009).
15. S. Stael, B. Wurzinger, A. Mair, N. Mehlmer, U. C. Vothknecht, M. Teige, Plant organellar calcium signalling: An emerging field. *J. Exp. Bot.* **63**, 1525–1542 (2012).
16. A. Costa, L. Navazio, I. Szabo, The contribution of organelles to plant intracellular calcium signalling. *J. Exp. Bot.* **69**, 4175–4193 (2018).
17. N. Pirayesh, M. Giridhar, A. Ben Khedher, U. C. Vothknecht, F. Chigri, Organellar calcium signaling in plants: An update. *Biochim. Biophys. Acta Mol. Cell Res.* **1868**, 118948 (2021).
18. F. Resentini, C. Ruberti, M. Grenzi, M. C. Bonza, A. Costa, The signatures of organellar calcium. *Plant Physiol.* **187**, 1985–2004 (2021).
19. M. Iwano, T. Entani, H. Shiba, M. Kakita, T. Nagai, H. Mizuno, A. Miyawaki, T. Shoji, K. Kubo, A. Isogai, S. Takayama, Fine-tuning of the cytoplasmic Ca^{2+} concentration is essential for pollen tube growth. *Plant Physiol.* **150**, 1322–1334 (2009).
20. E. Michard, P. T. Lima, F. Borges, A. C. Silva, M. T. Portes, J. E. Carvalho, M. Gilliham, L. H. Liu, G. Obermeyer, J. A. Feijó, Glutamate receptor-like genes form Ca^{2+} channels in pollen tubes and are regulated by pistil D-serine. *Science* **332**, 434–437 (2011).
21. G. B. Monshausen, M. A. Messerli, S. Gilroy, Imaging of the Yellow Cameleon 3.6 indicator reveals that elevations in cytosolic Ca^{2+} follow oscillating increases in growth in root hairs of *Arabidopsis*. *Plant Physiol.* **147**, 1690–1698 (2008).
22. A. Candeo, F. G. Doccula, G. Valentini, A. Bassi, A. Costa, Light sheet fluorescence microscopy quantifies calcium oscillations in root hairs of *Arabidopsis thaliana*. *Plant Cell Physiol.* **58**, 1161–1172 (2017).
23. G. J. Allen, J. M. Kwak, S. P. Chu, J. Llopis, R. Y. Tsien, J. F. Harper, J. I. Schroeder, Cameleon calcium indicator reports cytoplasmic calcium dynamics in *Arabidopsis* guard cells. *Plant J.* **19**, 735–747 (1999).
24. Y. Yang, A. Costa, N. Leonhardt, R. S. Siegel, J. I. Schroeder, Isolation of a strong *Arabidopsis* guard cell promoter and its potential as a research tool. *Plant Methods* **4**, 6 (2008).
25. L. Tian, S. A. Hires, T. Mao, D. Huber, M. E. Chiappe, S. H. Chalasani, L. Petreanu, J. Akerboom, S. A. McKinney, E. R. Schreiter, C. I. Bargmann, V. Jayaraman, K. Svoboda, L. L. Looger, Imaging neural activity in worms, flies and mice with improved GCaMP calcium indicators. *Nat. Methods* **6**, 875–881 (2009).
26. Y. Zhao, S. Araki, J. Wu, T. Teramoto, Y. F. Chang, M. Nakano, A. S. Abdelfattah, M. Fujiwara, T. Ishihara, T. Nagai, R. E. Campbell, An expanded palette of genetically encoded Ca^{2+} indicators. *Science* **333**, 1888–1891 (2011).
27. E. C. Greenwald, S. Mehta, J. Zhang, Genetically encoded fluorescent biosensors illuminate the spatiotemporal regulation of signaling networks. *Chem. Rev.* **118**, 11707–11794 (2018).

28. N. F. Keinath, R. Waadt, R. Brugman, J. I. Schroeder, G. Grossmann, K. Schumacher, M. Krebs, Live cell imaging with R-GECO1 sheds light on flg22- and chitin-induced transient [Ca^{2+}]cyt patterns in *Arabidopsis*. *Mol. Plant* **8**, 1188–1200 (2015).
29. T. A. DeFalco, M. Toyota, V. Phan, P. Karia, W. Moeder, S. Gilroy, K. Yoshioka, Using GCaMP3 to study Ca^{2+} signaling in *Nicotiana* species. *Plant Cell Physiol.* **58**, 1173–1184 (2017).
30. T. R. Vincent, M. Avramova, J. Canham, P. Higgins, N. Bilkey, S. T. Mugford, M. Pitino, M. Toyota, S. Gilroy, A. J. Miller, S. A. Hogenhout, D. Sanders, Interplay of plasma membrane and vacuolar ion channels, together with BAK1, elicits rapid cytosolic calcium elevations in *Arabidopsis* during aphid feeding. *Plant Cell* **29**, 1460–1479 (2017).
31. C. T. Nguyen, A. Kurenda, S. Stolz, A. Chételat, E. E. Farmer, Identification of cell populations necessary for leaf-to-leaf electrical signaling in a wounded plant. *Proc. Natl. Acad. Sci. U.S.A.* **115**, 10178–10183 (2018).
32. M. Toyota, D. Spencer, S. Sawai-Toyota, W. Jiaqi, T. Zhang, A. J. Koo, G. A. Howe, S. Gilroy, Glutamate triggers long-distance, calcium-based plant defense signaling. *Science* **361**, 1112–1115 (2018).
33. F. Resentini, M. Grenzi, D. Ancora, M. Cademartori, L. Luoni, M. Franco, A. Bassi, M. C. Bonza, A. Costa, Simultaneous imaging of ER and cytosolic Ca^{2+} dynamics reveals long-distance ER Ca^{2+} waves in plants. *Plant Physiol.* **187**, 603–617 (2021).
34. M. Grenzi, S. Buratti, A. S. Parmagnani, I. Abdel Aziz, I. Bernacka-Wojcik, F. Resentini, J. Šimura, F. G. Doccula, A. Alfieri, L. Luoni, K. Ljung, M. C. Bonza, E. Stavrinidou, A. Costa, Long-distance turgor pressure changes induce local activation of plant glutamate receptor-like channels. *Curr. Biol.* **33**, 1019–1035.e8 (2023).
35. C. Yan, Q. Gao, M. Yang, Q. Shao, X. Xu, Y. Zhang, S. Luan, Ca^{2+}/calmodulin-mediated desensitization of glutamate receptors shapes plant systemic wound signalling and anti-herbivore defence. *Nat. Plants* **10**, 145–160 (2024).
36. Y. Fichman, R. Mittler, Rapid systemic signaling during abiotic and biotic stresses: Is the ROS wave master of all trades? *Plant J.* **102**, 887–896 (2020).
37. R. Li, Y. Yang, H. Lou, W. Wang, J. Yan, D. Xie, X. Shan, Electrical and calcium signaling in plant systemic defense: From local wounds to global responses. *New Phytol.* **247**, 1633–1642 (2025).
38. T. C. Xiong, E. Ronzier, F. Sanchez, C. Corratgé-Faillie, C. Mazars, J.-B. Thibaud, Imaging long distance propagating calcium signals in intact plant leaves with the BRET-based GFP-aequorin reporter. *Front. Plant Sci.* **5**, 43 (2014).
39. V. Kiep, J. Vadassery, J. Lattke, J. P. Maaß, W. Boland, E. Peiter, A. Mithöfer, Systemic cytosolic Ca^{2+} elevation is activated upon wounding and herbivory in *Arabidopsis*. *New Phytol.* **207**, 996–1004 (2015).
40. W. G. Choi, M. Toyota, S. H. Kim, R. Hilleary, S. Gilroy, Salt stress-induced Ca^{2+} waves are associated with rapid, long-distance root-to-shoot signaling in plants. *Proc. Natl. Acad. Sci. U.S.A.* **111**, 6497–6502 (2014).
41. X. Zhao, Y. L. Wang, X. R. Qiao, J. Wang, L. D. Wang, C. S. Xu, X. Zhang, Phototropins function in high-intensity blue light-induced hypocotyl phototropism in *Arabidopsis* by altering cytosolic calcium. *Plant Physiol.* **162**, 1539–1551 (2013).
42. C. Weigand, S.-H. Kim, E. Brown, E. Medina, M. Mares III, G. Miller, J. F. Harper, W.-G. Choi, A ratiometric calcium reporter CGf reveals calcium dynamics both in the single cell and whole plant levels under heat stress. *Front. Plant Sci.* **12**, 777975 (2021).
43. M. R. Ishka, E. Brown, A. Rosenberg, S. Romanowsky, J. A. Davis, W. G. Choi, J. F. Harper, *Arabidopsis* Ca^{2+}-ATPases 1, 2, and 7 in the endoplasmic reticulum contribute to growth and pollen fitness. *Plant Physiol.* **185**, 1966–1985 (2021).
44. M. J. Evans, R. J. Morris, Chemical agents transported by xylem mass flow propagate variation potentials. *Plant J.* **91**, 1029–1037 (2017).
45. E. E. Farmer, Y. Q. Gao, G. Lenzoni, J. L. Wolfender, Q. Wu, Wound- and mechanostimulated electrical signals control hormone responses. *New Phytol.* **227**, 1037–1050 (2020).
46. E. Tinturier, É. Badel, N. Leblanc-Fournier, J. L. Julien, Stem bending generates electrical response in poplar. *Physiol. Plant.* **173**, 954–960 (2021).
47. V. Bacheva, F. E. Rockwell, J. B. Salmon, J. D. Woodson, M. H. Frank, A. D. Stroock, A unified framework for hydromechanical signaling can explain transmission of local and long-distance signals in plants. *Proc. Natl. Acad. Sci. U.S.A.* **122**, e2422692122 (2025).
48. U. Ricca, Soluzione d'un problema di fisiologia: La propagazione di stimolo nella "Mimosa". *Nuovo Giorn. Bot. Ital.* **23**, 51–170 (1916).
49. J. W. V. Van Sambeek, B. G. Pickard, C. E. Ulbright, Mediation of rapid electrical, metabolic, transpirational, and photosynthetic changes by factors released from wounds. II. Mediation of the variation potential by Ricca's factor. *Can. J. Bot.* **54**, 2651–2661 (1976).
50. M. Malone, B. Stanković, Surface potentials and hydraulic signals in wheat leaves following localized wounding by heat. *Plant Cell Environ.* **14**, 431–436 (1991).
51. B. Stanković, D. L. Witters, T. Zawadzki, E. Davies, Action potentials and variation potentials in sunflower: An analysis of their relationships and distinguishing characteristics. *Physiol. Plant.* **103**, 51–58 (1998).
52. M. R. Zimmermann, H. H. Felle, Dissection of heat-induced systemic signals: Superiority of ion fluxes to voltage changes in substomatal cavities. *Planta* **229**, 539–547 (2009).
53. V. Vodeneev, A. Orlova, E. Morozova, L. Orlova, E. Akinchits, O. Orlova, V. Sukhov, The mechanism of propagation of variation potentials in wheat leaves. *J. Plant Physiol.* **169**, 949–954 (2012).
54. S. A. Mousavi, A. Chauvin, F. Pascaud, S. Kellenberger, E. E. Farmer, *GLUTAMATE RECEPTOR-LIKE* genes mediate leaf-to-leaf wound signalling. *Nature* **500**, 422–426 (2013).
55. A. Alfieri, F. G. Doccula, R. Pederzoli, M. Grenzi, M. C. Bonza, L. Luoni, A. Candeo, N. Romano Armada, A. Barbiroli, G. Valentini, T. R. Schneider, A. Bassi, M. Bolognesi, M. Nardini, A. Costa, The structural bases for agonist diversity in an *Arabidopsis thaliana* glutamate receptor-like channel. *Proc. Natl. Acad. Sci. U.S.A.* **117**, 752–760 (2020).
56. A. Bellandi, D. Papp, A. Breakspear, J. Joyce, M. G. Johnston, J. de Keijzer, E. C. Raven, M. Ohtsu, T. R. Vincent, A. J. Miller, D. Sanders, S. A. Hogenhout, R. J. Morris, C. Faulkner, Diffusion and bulk flow of amino acids mediate calcium waves in plants. *Sci. Adv.* **8**, eabo6693 (2022).
57. J. S. Marvin, B. G. Borghuis, L. Tian, J. Cichon, M. T. Harnett, J. Akerboom, A. Gordus, S. L. Renninger, T. W. Chen, C. I. Bargmann, M. B. Orger, E. R. Schreiter, J. B. Demb, W. B. Gan, S. A. Hires, L. L. Looger, An optimized fluorescent probe for visualizing glutamate neurotransmission. *Nat. Methods* **10**, 162–170 (2013).
58. A. Aggarwal, R. Liu, Y. Chen, A. J. Ralowicz, S. J. Bergerson, F. Tomaska, B. Mohar, T. L. Hanson, J. P. Hasseman, D. Reep, G. Tsegaye, P. Yao, X. Ji, M. Kloos, D. Walpita, R. Patel, M. A. Mohr, P. W. Tillberg, GENIE Project Team, L. L. Looger, J. S. Marvin, M. B. Hoppa, A. Konnerth, D. Kleinfeld, E. R. Schreiter, K. Podgorski, Glutamate indicators with improved activation kinetics and localization for imaging synaptic transmission. *Nat. Methods* **20**, 925–934 (2023).
59. A. Aggarwal, A. Negrean, Y. Chen, R. Iyer, D. Reep, A. Liu, A. Palutla, M. E. Xie, B. J. MacLennan, K. M. Hagihara, L. W. Kinsey, J. L. Sun, P. Yao, J. Zheng, A. Tsang, G. Tsegaye, Y. Zhang, R. H. Patel, B. J. Arthur, J. Hiblot, P. Leippe, M. Tarnawski, J. S. Marvin, J. D. Vevea, S. C. Turaga, A. G. Tebo, M. Carandini, L. F. Rossi, D. Kleinfeld, A. Konnerth, K. Svoboda, G. C. Turner, J. Hasseman, K. Podgorski, Glutamate indicators with increased sensitivity and tailored deactivation rates. *Nat. Methods* 10.1038/s41592-025-02965-z (2025).
60. Food and Agriculture Organization of the United Nations (FAO), "Climate change and food security: A framework document" (FAO, 2008).
61. A. Bakshi, W.-G. Choi, S.-H. Kim, S. Gilroy, The vacuolar Ca^{2+} transporter CATION EXCHANGER 2 regulates cytosolic calcium homeostasis, hypoxic signaling, and response to flooding *in Arabidopsis thaliana*. *New Phytol.* **240**, 1830–1847 (2023).
62. M. Á. Peláez-Vico, A. Tukuli, P. Singh, D. G. Mendoza-Cózatl, T. Joshi, R. Mittler, Rapid systemic responses of *Arabidopsis* to waterlogging stress. *Plant Physiol.* **193**, 2215–2231 (2023).
63. T. Rankenberg, H. van Veen, M. Sedaghatmehr, C. Y. Liao, M. B. Devaiah, E. A. Stouten, S. Balazadeh, R. Sasidharan, Differential leaf flooding resilience in *Arabidopsis thaliana* is controlled by ethylene signaling-activated and age-dependent phosphorylation of ORESARA1. *Plant Commun.* **5**, 100848 (2024).
64. Y. Muraoka, M. Ueda, Nyctinasty. *Curr. Biol.* **34**, R307–R308 (2024).
65. S. Pei, Y. Liu, W. Li, B. Krichilsky, S. Dai, Y. Wang, X. Wang, D. M. Johnson, B. M. Crawford, G. B. Swift, T. Vo-Dinh, Z. M. Pei, F. Yuan, OSCA1 is an osmotic specific sensor: A method to distinguish Ca^{2+}-mediated osmotic and ionic perception. *New Phytol.* **235**, 1665–1678 (2022).
66. H. Suda, H. Mano, M. Toyota, K. Fukushima, T. Mimura, I. Tsutsui, R. Hedrich, Y. Tamada, M. Hasebe, Calcium dynamics during trap closure visualized in transgenic Venus flytrap. *Nat. Plants* **6**, 1219–1224 (2020).
67. T. Hagihara, H. Mano, T. Miura, M. Hasebe, M. Toyota, Calcium-mediated rapid movements defend against herbivorous insects in Mimosa pudica. *Nat. Commun.* **13**, 6412 (2022).
68. J. M. Christie, M. D. Zurbriggen, Optogenetics in plants. *New Phytol.* **229**, 3108–3115 (2021).
69. J. H. Rowe, M. Grangé-Guermente, M. Exposito-Rodriguez, R. Wimalasekera, M. O. Lenz, K. N. Shetty, S. R. Cutler, A. M. Jones, Next-generation ABACUS biosensors reveal cellular ABA dynamics driving root growth at low aerial humidity. *Nat. Plants* **9**, 1103–1115 (2023).
70. A. Rizza, A. Walia, V. Lanquar, W. B. Frommer, A. M. Jones, In vivo gibberellin gradients visualized in rapidly elongating tissues. *Nat. Plants* **3**, 803–813 (2017).
71. B. Tang, J. Lu, H. Leontovyčová, G. Hoffmann, J. H. Rowe, S. F. O'Donnell, M. Grangé-Guermente, B. Larsen, R. Wimalasekera, P. Carella, M. Incarbone, T. Kalachova, A. M. Jones, SALICYLIC ACID SENSOR1 reveals the propagation of an SA hormone surge during plant pathogen advance. *Science* **390**, 188–194 (2025).
72. R. B. Horsch, J. E. Fry, N. L. Hoffmann, D. Eichholtz, S. G. Rogers, R. T. Fraley, A simple and general method for transferring genes into plants. *Science* **227**, 1229–1231 (1985).
73. T. Murashige, F. Skoog, A revised medium for rapid growth and bio assays with tobacco tissue cultures. *Physiol. Plant.* **15**, 473–497 (1962).

Acknowledgments: We thank M. Toyota (Saitama University, Japan) for providing us with the *35S::CHIB-iGluSnFR* construct used to transform *N. benthamiana* plants, D. Sanders (John Innes Centre, Norwich, UK) for providing us with the GCaMP3 *A. thaliana* plants, and NOLIMITS Nikon Imaging Center of Excellence for Plant Biology and Other Life Sciences, established by the University of Milan and the "Piattaforma piante" at the Department of Biosciences of the University of Milan. We thank M. Casartelli and S. Caccia for assistance with the *S. littoralis*

larvae. **Funding:** This work was supported by Ministero dell'Istruzione, dell'Università e della Ricerca (Fondo per Progetti di Ricerca di Rilevante Interesse Nazionale 2022, PRIN 2022NMSFHN) (to A.Co. and S.B.); Agritech National Research Center, funded by the European Union NextGenerationEU [Piano Nazionale di Ripresa e Resilienza (PNRR) - Missione 4, Componente 2, Investimento 1.4 - D.D. 1032 17/06/2022; CN00000022 - CUP D43C22001350001] (to A.B., A.Ca., A.Co., and B.M.O.M.); University of Milan and the Department of Biosciences for providing the Assegno di Ricerca Tipo A (postdoctoral fellowship) (to M.G.); and Chan Zucherber Initiative (napari Plugin Foundation, grant number 310442, to A.B. and G.T.). We thank the Fratelli Confalonieri Foundation for providing a postdoctoral research fellow (to S.B.). **Author contributions:** Conceptualization: A.Co. and A.B. Methodology: A.B., A.Ca., G.T., and S.B. Investigation: A.B., B.M.O.M., G.T., and M.G. Visualization: A.Co., G.T., B.M.O.M., and V.C. Data curation: A.B., G.T., and B.M.O.M. Supervision: A.Co. and A.B. Resources: L.L., S.B., and K.Y. Writing—original draft: A.Co., A.B., G.T., and B.M.O.M. Writing—review and editing: A.Co., A.B., A.Ca., and K.Y. Funding acquisition: A.Co., A.B., and S.B. Validation: A.Co., A.B., and K.Y. Formal analysis: A.Co., A.B., G.T., and B.M.O.M. Software: A.B. and G.T. Project administration: A.Co. and A.B. **Competing interests:** The authors declare that they have no competing interests. **Data and materials availability:** All data and code needed to evaluate and reproduce the results in the paper are present in the paper and/or the Supplementary Materials. The raw data for the images presented in the manuscript and the code to run the MAPPI system are available on Zenodo (https://doi.org/10.5281/zenodo.15845576). The code to run the MAPPI system is also available on the dedicated GitHub repository (https://github.com/micropolimi/MAPPI) along with the code used to analyze the data.

Submitted 11 July 2025
Accepted 23 December 2025
Published 23 January 2026
10.1126/sciadv.aea4466

ScienceAdvances

MAcro Plant Projection Imaging (MAPPI): An open, scalable platform for whole-plant fluorescence real-time imaging

Giorgia Tortora, Bianca Maria Orlando Marchesano, Stefano Buratti, Laura Luoni, Matteo Grenzi, Keiko Yoshioka, Valeria Contartese, Alessia Candeo, Alex Costa, and Andrea Bassi

Sci. Adv. **12** (4), eaea4466. DOI: 10.1126/sciadv.aea4466

Science Advances (ISSN 2375-2548) is published by the American Association for the Advancement of Science. 1200 New York Avenue NW, Washington, DC 20005. The title *Science Advances* is a registered trademark of AAAS.